J. Fluid Mech. (1997), *vol.* 346, *pp.* 77–115. Printed in the United Kingdom

On the structure of bow waves on a ship model

By RONALD R. DONG[1], JOSEPH KATZ[1] AND THOMAS T. HUANG[2]

[1] Department of Mechanical Engineering, The Johns Hopkins University, Baltimore, MD 21218, USA

[2] NSWC/Carderock Division – David Taylor Model Basin, Bethesda, MD 20084, USA

(Received 17 April 1996 and in revised form 26 December 1996)

Particle image velocitmetry (PIV) measurements and free-surface visualizations around a ship model focus on the flow within the attached liquid sheet, upstream of the point at which the bow wave separates from the model, the origin and structure of the bow wave and the flow downstream of the wave crest. The measurements are performed at Reynolds numbers ranging between 2.8×10^6 and 7.4×10^6 and Froude numbers between 0.17 and 0.45 (both are based on ship length L). Representative velocity and vorticity distributions at $Fr_L = 0.28$ and $Fr_L = 0.45$ demonstrate the characteristic structure of mild and steep waves, respectively. Very close to the bow the attached sheet is thin and quite unsteady. With increasing distance from the nose the sheet becomes thicker and its development involves considerable vorticity production. In the mild case this vorticity is originated at the free surface, whereas in the steep wave case, boundary layer separation occurs on the model, which also transports vorticity into the sheet. This vorticity and its associated induced lateral flow remain near the model downstream of the bow wave. By calculating the acceleration component tangent to the free surface of the sheet it is shown that the peaks in the near-surface vorticity appear in regions with high viscous flux of vorticity from the surface. Formation of a bow wave also involves considerable production of vorticity. Similar to two-dimensional breakers, the primary origin of this vorticity is at the toe of the breaker. However, unlike the two-dimensional cases, the region containing vorticity in the ship wave does not appear as an extended shear layer. Instead, this vorticity is convected out of the plane of the laser sheet in a series of distinct vortex filaments. The ship wave also has powerful counter-rotating vorticity concentrated near the wave crest that has been observed in two-dimensional waves, but not of the same strength. Breaking becomes weaker, i.e. there is less vorticity production, with increasing distance from the model, but it persists even at the 'tail' of the bow wave. The sites of vorticity entrainment of both signs are consistent with the computed near-surface acceleration. Estimates of the three-dimensional velocity distribution and head losses within the wave are also provided.

1. Introduction

Very few experimental data are available on the flow structure within the liquid sheet developing around the bow of a ship and on the intersection of this sheet with the main bow wave. The structure of the wave, however, has received considerable attention, as summarized in a comprehensive review by Miyata & Inui (1984). Using aluminium powder they observed that the near-surface flow structure and wave pattern depended strongly on the Froude number and configuration of the bow. They also demonstrated that the near-surface flow became turbulent downstream of the wave crest. Velocity

measurements, using Pitot tubes, showed that this transition involved significant energy loss and abrupt change in flow direction. The velocity component normal to the wave decreased significantly, whereas the parallel component remains almost unchanged. Based on this observation they made an analogy between bow waves and oblique shocks. Experiments with different model draught and the same overall length demonstrated also that in most cases the dominating length scale was the ship draught. Limitations inherent to their measurement technique meant that Miyata & Inui did not probe the liquid sheet upstream of the main bow wave and stayed away from the immediate vicinity of the wall and the free surface. These domains are the foci of the present paper.

Unlike ship waves, the flow structure within two-dimensional spilling breakers has been investigated extensively. The onset of wave breaking was studied theoretically by Longuet Higgins (1992, 1994), experimentally by Duncan *et al.* (1994) and numerically by Dommermuth & Mui (1994). Their conclusions are discussed and compared to the present observations in §4.2. Recent particle image velocimetry (PIV) measurements by Lin & Rockwell (1994, 1995) and by Dabiri & Gharib (1997) demonstrated that wave breaking caused the formation of an extended shear layer that originated at the toe of the wave. Lin & Rockwell (1995) also showed that the structure and strength of this layer depended on the Froude number and that the initiation of breaking from capillary waves agreed with Longuet Higgins (1992, 1994) and Duncan *et al.* (1994). The extent and role turbulence in this mixing layer were discussed by Hoyt & Sellin (1989), Banner & Peregrine (1993) and Cointe & Tulin (1994). The origin of vorticity within the wave and its relationship to the flow near the surface and shape of the wave were addressed by Rood (1994, 1995) and Dabiri & Gharib (1997). They showed, as the present experiments in ship waves will also confirm, the significance of viscous diffusion of vorticity from the free surface. The complex structure of plunging and steep waves was studied by Dommermuth *et al.* (1988) and Melville & Rapp (1988). Further details and many more references can be found in review articles by Peregrine & Svendsen (1978) and Banner & Peregrine (1993).

In the present study we focus on the flow and wave structure near the bow of a ship model. Included are the liquid sheet attached to the bow, the flow structure within the bow wave at different distances from the ship model, particularly the flow very close to the free surface, the mechanisms of vorticity production and the extent of energy losses. PIV is used for measuring the velocity and vorticity distributions and the results are compared to the structure of two-dimensional breaking waves. As far as the flow structure within the liquid sheet and its impact on the flow downstream is concerned, to the best of our knowledge the data in this paper are unique. The experimental set-up and analysis procedures are discussed in §2 that follows. Results, including photographs, velocity and vorticity distributions within the liquid sheet, mild and steep breaking bow waves are presented in §3. Similarities to and differences from two-dimensional waves are introduced and discussed. Section 4.1 contains estimates of the three-dimensional velocity distributions and head losses due to wave breaking. The origin of vorticity within the ship wave and its relationship to the flow near the free surface, all based on the experimental data, are discussed in §4.2.

2. Experimental set-up and analysis procedures

The experiments were performed in the 140 ft towing basin at the David Taylor Model Basin. The ship model was a rigidly attached, 3.05 m long, 10.4 cm draught model no. 4817 (see figure 1*a*). Velocity measurements were performed using PIV and

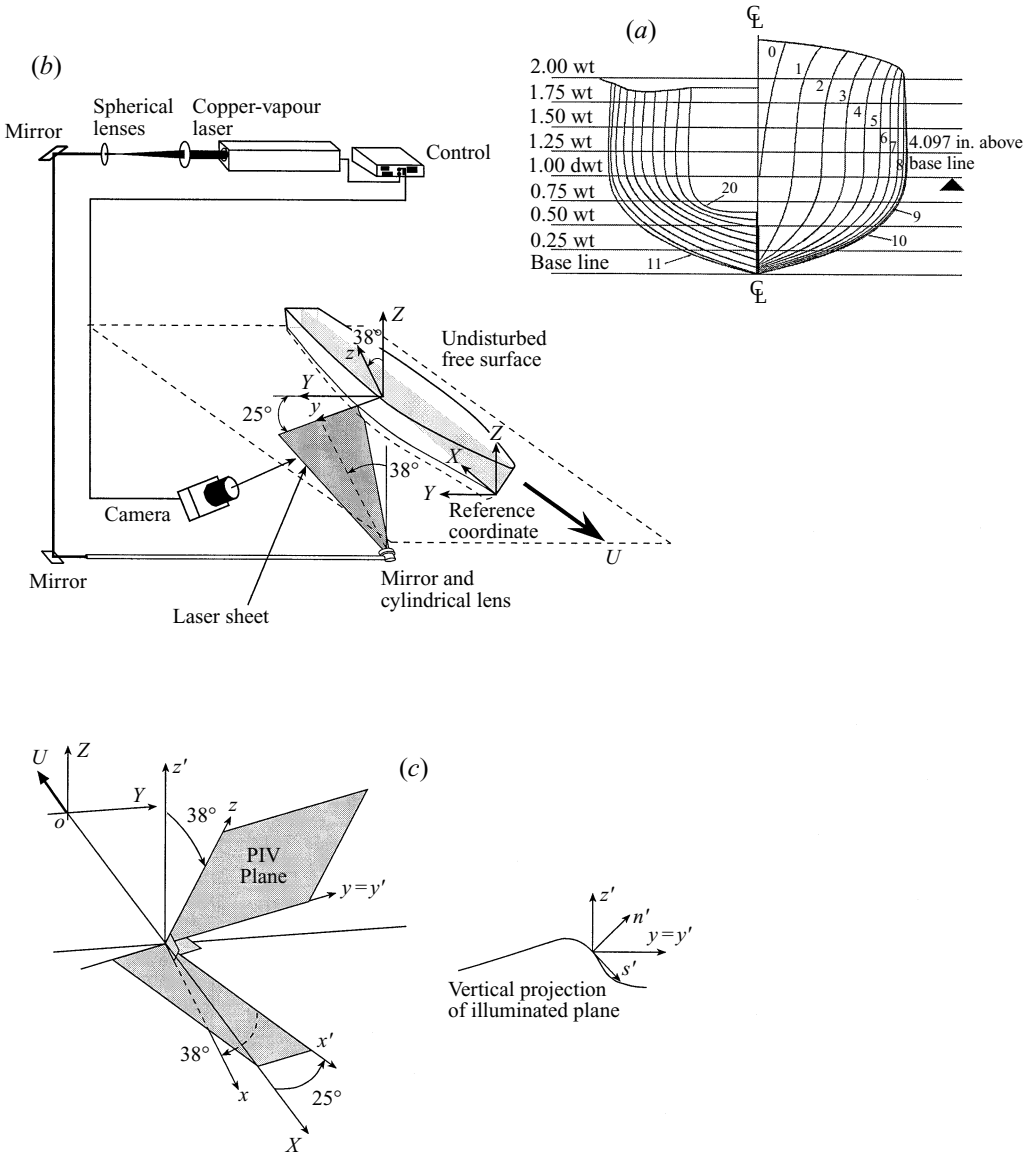

FIGURE 1. (*a*) The layout of ship model 4817 (series 64). (*b*) Schematic description of the experimental set-up in the 140 ft basin at DTMB. (*c*) Reference coordinates as seen by the camera, from behind.

the experimental set-up shown schematically in figure 1 (*b*). The light source was an air-cooled 15 W copper vapour laser. The timings of laser pulses were synchronized with the camera and ship location using an encoder mounted on the towing tank carriage and a PC-based control system. To resolve the flow within the entire wave structure it was necessary to illuminate flow field from below. The laser sheet was tilted by 25° to the direction of motion and by 38° to the vertical axis. The 25° angle was selected as a compromise between the orientations of the bow wave and the hull and allowed measurements up to the tip of the bow. The vertical tilt was essential for observations within the wave with a submerged camera. Its effect on the data and conclusions is discussed in detail in §4. Besides providing an unobstructed view this tilt has an additional benefit. By assuming that the velocity component normal to the surface, $u_{n'}$

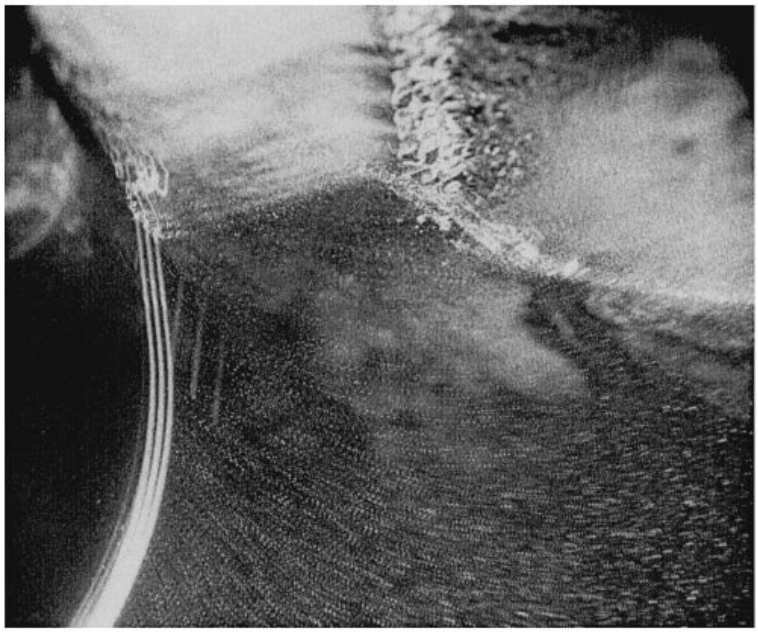

FIGURE 2. A sample photograph of PIV data at $X/L = 0.13$ and $Fr_L = 0.334$.

(figure 1*c*), is zero the tilted perspective allowed us to estimate all three components of the velocity on the free surface. Data were recorded with a 65 frames s^{-1}, 35 mm film camera equipped with a 90 mm lens, on a TMAX, ASA 3200 film that has a resolution of about 150 lines mm^{-1}. The actual recording rate was reduced to 10 frames s^{-1} to accommodate the required delay between exposures. Most of the data were recorded with three exposures per image, with delay between exposures ranging between 8 and 10 ms, depending on flow speed and location along the model. The tracer particles were 40–60 μm in diameter, neutrally buoyant (specific gravity between 0.95 and 1.05) and fluorescent (they respond at about 560 nm to green excitation, as described in Dong, Chu & Katz 1992). They were distributed in the water around the laser sheet (we did not seed the entire tank) several minutes prior to each run using a special rake. The flow induced by the rake was allowed to settle before towing the model, as the PIV images prior to the arrival of the model confirmed. A sample image showing the particle traces and intersection of the light sheet with the surface is shown in figure 2. The blurry white spots on the image were caused by reflection of the light sheet from the surface. Use of a colour filter that eliminated the green light solved part of the problem, but not completely, due to the presence of fluorescent particles in the reflected sheet. As is evident from this sample (and confirmed by video images), in the present laser sheet the flow is unidirectional and there is no need to deal with ambiguity.

The images were digitized with a Nikon LS3500 slide Scanner to arrays ranging between 3072×2048 pixels, under normal conditions, and 6144×4096 pixels, in 'difficult spots'. The images were enhanced to deal with background non-uniformities, and the velocity was computed using an in-house-developed auto-correlation software (Dong *et al.* 1992; Fu *et al.*1994; Roth, Hart & Katz 1995). The intersection lines of the light sheet with the model and with the free surface were removed from the image before computing the velocity. The interrogation window size was 64×64 pixels (3.5 mm^2) and the distance between adjacent windows was 32 pixels (50% overlap).

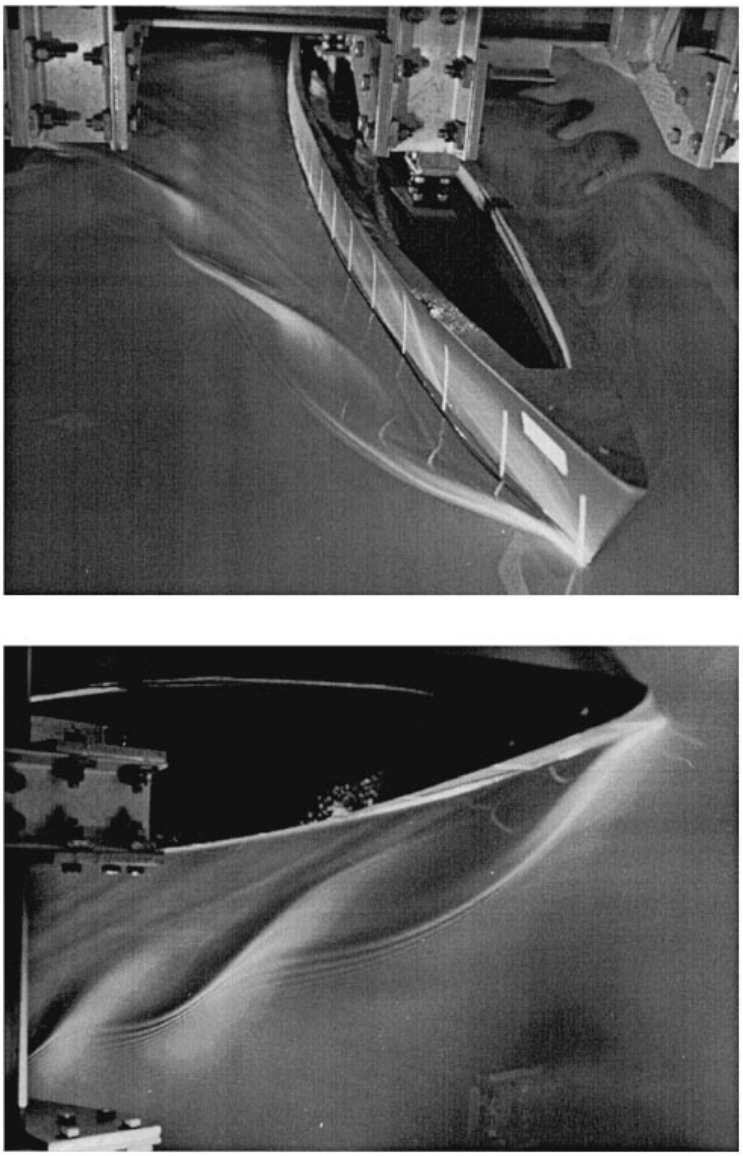

FIGURE 3. The wave structure around the ship at $Fr_L = 0.167$: (*a*) side view; (*b*) top view.

The typical uncertainty level was about 0.4 pixels (including the effects of image enhancement, as discussed in Roth *et al.* 1995), which, for a typical 20 pixels displacement, resulted in a characteristic error of 2 %. The resulting typical uncertainty in vorticity was in the 10 %–20 % range. Further detailed discussion on PIV can be found in Adrian (1991). The surface contour in each illuminated plane was also determined from the digitized images by measuring the location of the intersection of the light sheet with the surface. We used the middle line, i.e. the intersection during the second exposure. Since this plane was inclined by 38°, the actual vertical elevation of the water was only 79 % of values measured from the PIV images.

(*a*)

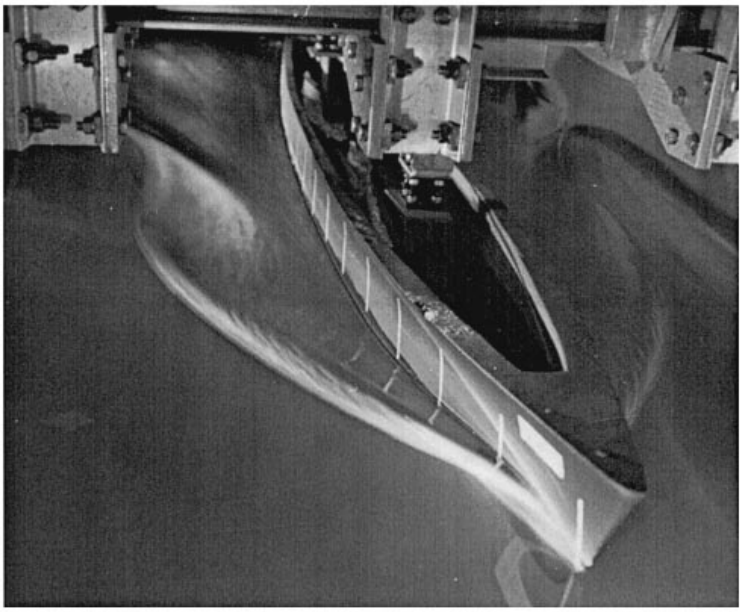

(*b*)

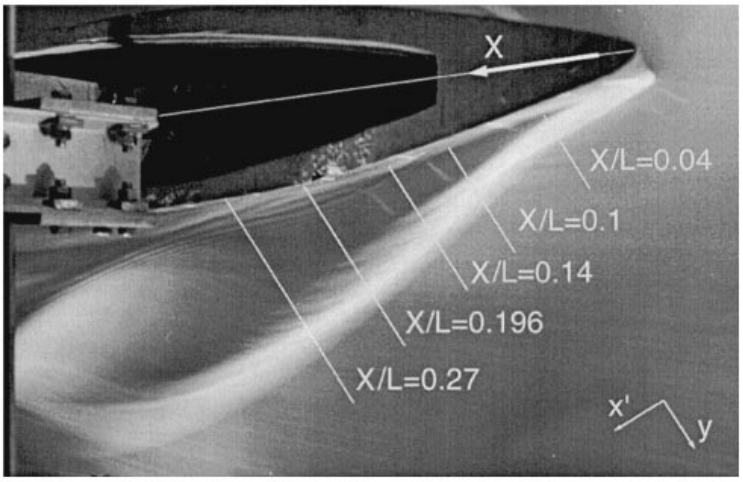

FIGURE 4(*a*, *b*). For caption see facing page.

3. Results

3.1. *Observations above the surface*

Top-view photographs of the surface wave structure are presented in figures 3–6 for Froude numbers ($Fr_L = U/(gL)^{1/2}$, where U and L are the ship speed and length, respectively) of 0.17, 0.28, 0.33 and 0.45, respectively. The corresponding Froude numbers based on the draught, Fr_D, are 0.9, 1.5, 1.8 and 2.4 (the draught of the vertical length of the submerged portion of the ship). Here $L = 3.05$ m and $U = 0.914$–2.44 m s^{-1}. These extended-exposure images, using a camera mounted on the carriage, were recorded by spreading fine aluminium powder on the surface. By repeating the experiments with varying powder concentrations, we verified that the powder did not have a major effect on the overall wave structure. As is evident from

(*c*)

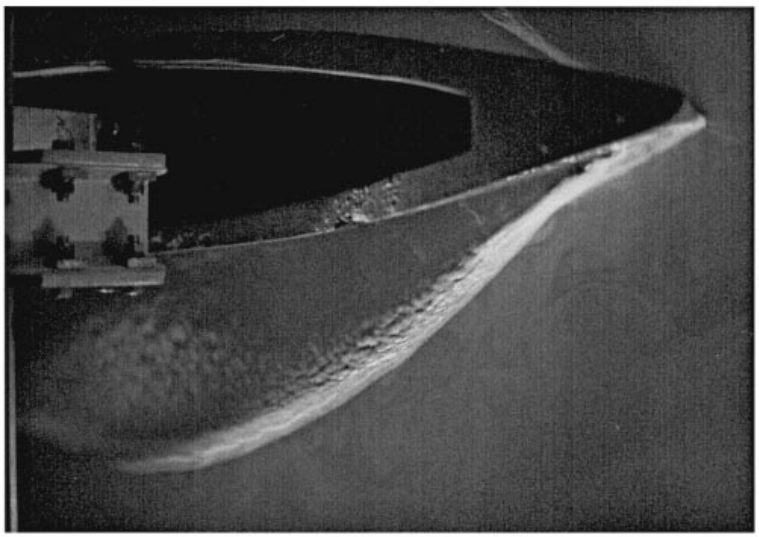

FIGURE 4. The wave structure around the ship at $Fr_L = 0.279$: (*a*) side view; (*b*) top view including the location of the laser sheets; (*c*) a short-exposure image aimed at illustrating the onset of free-surface turbulence in the bow wave.

the results, with increasing Froude number the angle between the bow wave and the model axis decreases, the point along the body at which the wave detaches from the model moves further downstream, the distance between waves increases, and the wave crests become straighter (less curved). These trends are consistent with observations reported by Miyata & Inui (1984) on other ship models.

Also evident from the photographs is the formation of a thin liquid sheet on the body upstream of the point at which the bow wave clearly separates from the model. The shape and behaviour of this sheet was examined using a video camera mounted above the surface (see the sample image in figure 7). Very close to the nose (bow) the sheet is very thin, not more that 2 mm wide, and is quite unsteady, fluctuating in elevation and thickness. In some cases the upper portion of this thin film seems to roll up, giving it a 'bumpy' appearance, as figures 5(*c*) and 7 clearly show. One of the velocity distributions (figure 13) presented in this paper dissects this thin sheet close to its origin. Another curious phenomenon, which will be discussed later, is the apparent formation of distinct filaments that extend from the forward face of the wave into the flow behind it. They are particularly evident in figures 5 and 6 and to a lesser extent in figure 4. Also evident (figures 4*b* and 5*b*) is the tendency of the flow downstream of the bow wave crest to turn towards the body and then turn outwards again as it reaches the next wave crest. The latter outward trend has also been demonstrated by Miyata & Inui (1984), as part of their attempt to make an analogy between a bow wave and an oblique shock. On a surface-piercing body with a long draught (Pogozelski, Katz & Huang 1996) the inward flow impinges on the body (the next wave is formed further downstream), causing the generation of a bubbly wake. This series of extended-exposure photographs also indicates that the main features of the flow, i.e. wave shape, configuration and location of filaments and main trends in flow direction, are quite steady. However, in most cases the near-surface flow becomes turbulent while crossing the wave (figure 4*c*), in agreement with Miyata & Inui for ship waves as well as Peregrine & Svendsen (1978) for two-dimensional waves. Before concluding this subsection, note that the streaks in figure 6(*b*), beyond the $X/L = 0.24$ line, have been

(*a*)

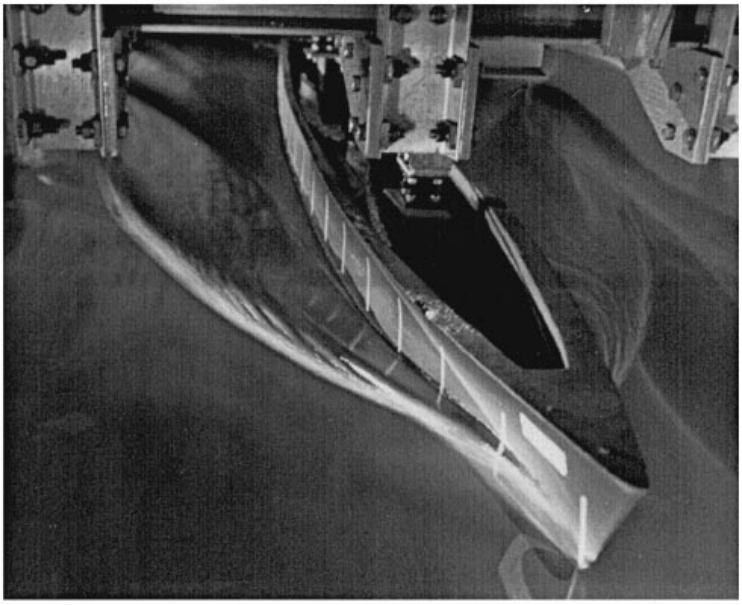

(*b*)

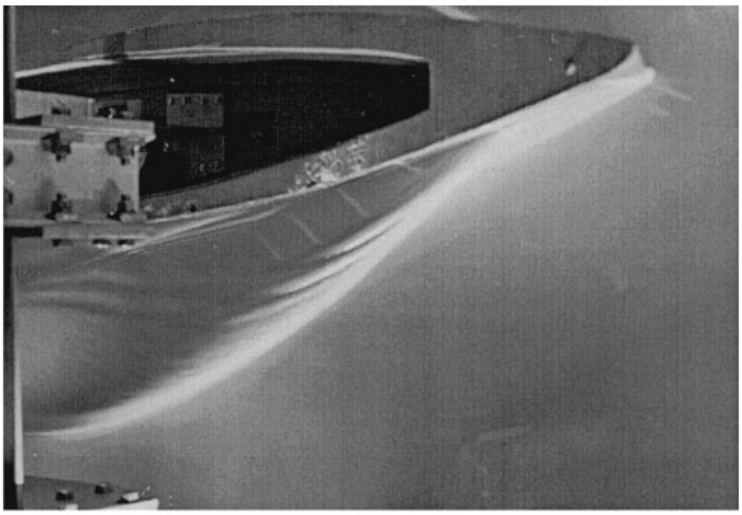

FIGURE 5(*a*, *b*). For caption see facing page.

created by entrained bubbles. At lower Froude numbers and upstream of this line the bubble entrainment is minimal.

Sample velocity and vorticity distributions for Fr_D of 1.51 and 2.41 are presented in figures 8–16. The first series, at $Fr_D = 1.51$, represents a flow with a mild-crested bow wave, and the second series, at $Fr_D = 2.41$, represents a steep bow wave, that at a certain distance further away from the body plunges and generates a bubbly wake. Note that the exact locations and extent of the visualized planes are marked in figures 4(*b*) and 6(*b*).

3.2. *Bow wave with a mild slope*

Figures 8–12 contain sample data for the relatively mild case ($Fr_L = 0.279$). All are observed with the set-up and camera orientation presented in figure 2(*b*). Figure 8

(*c*)

FIGURE 5. The wave structure around the ship at $Fr_L = 0.334$: (*a*) side view; (*b*) top view; (*c*) the liquid film around the bow.

shows the velocity and vorticity distributions at the end of the liquid sheet, just as the bow wave starts separating from the body (the exact location is marked in figure 4*b*). At this location the liquid sheet forming around the bow reaches a maximum elevation of $z/L = 0.0149$ ($z = 0$ is the undisturbed elevation of the free surface) at $X/L = 0.04$. Recall that the actual elevation of the surface is only 79% of the values indicated in the vector maps since the light sheet is inclined. Near the crest of the liquid sheet, where the flow has already started turning downward, the maximum velocity exceeds 20% of the model speed. Below the liquid sheet the velocity gradually decreases to 18% at $z/L = 0$ and 16% at $z/L = -0.007$. Close to $z/L = -0.0135$, which is still 59% of the draught above the ship bottom, w changes sign. Note that at this depth the streamwise velocity outside the boundary layer (which is very thin, much smaller than an interrogation window at this location) is quite small. Thus, when w changes sign, w', the vertical velocity component, also becomes negative at a nearby location. The flow below this point is displaced below the ship and the flow above, which is pushed upward, is involved in the wave motion. The existence of such saddle points on the surface of the model has been observed by Fry & Kim (1984) while performing laser Doppler velocimetry measurements on a different ship model.

Close to the 'toe' of the liquid sheet (around $y/L = 0.0173$) the velocity turns upward and then decreases rapidly from 18% at $y/L = 0.0173$ to 10% at $y/L = 0.0234$. This region marks the intersection of the sheet with the forward face of the main bow wave. The vorticity distribution (figure 8*b*) contains mostly negative peaks that start very close to the surface near the toe, but extend into the liquid, away from the surface with increasing y/L. There is also a weak but distinct positive peak close to the crest of the liquid sheet. As will be shown later, these phenomena are much more pronounced at $Fr_L = 0.45$ (figures 13–16), and will be discussed when these data are presented.

Further downstream, at $X/L = 0.1$ (figure 9), the crest of the bow wave has already separated from the body. On the entire forward (right) face of this wave, starting from the toe, the vorticity is negative. Just below the wave crest the negative vorticity extends into the liquid, where it borders fluid with positive vorticity on both sides. The entire

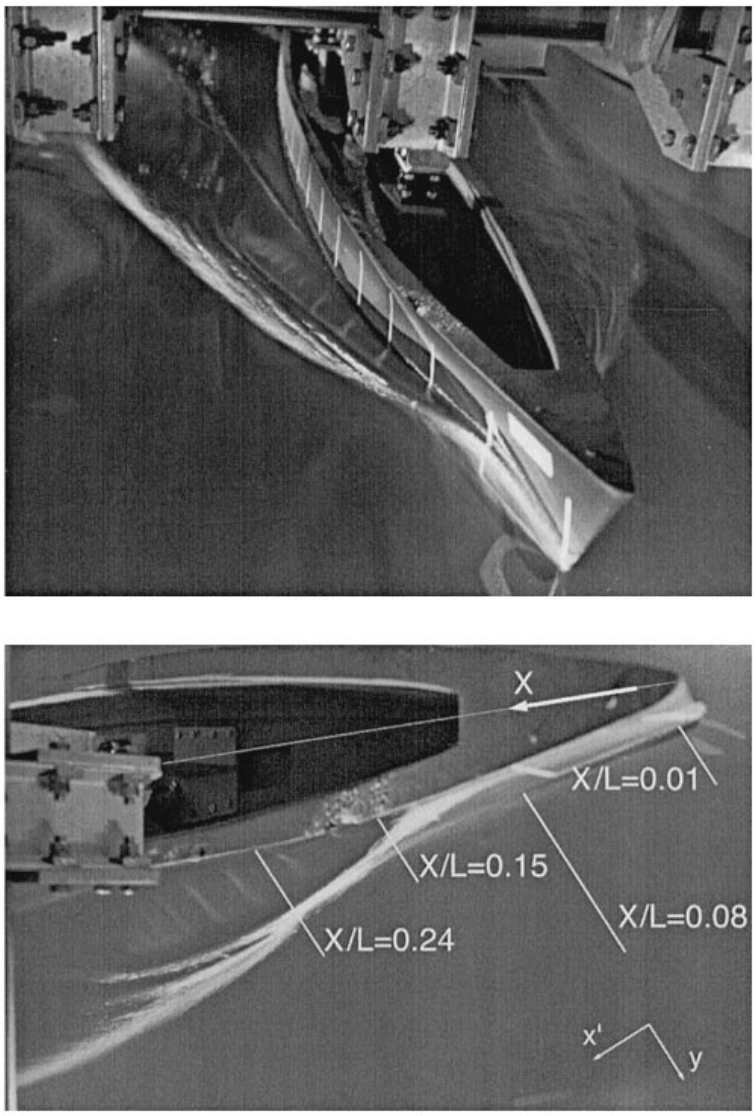

FIGURE 6. The wave structure around the ship at $Fr_L = 0.446$: (*a*) side view; (*b*) top view including the location of the laser sheets.

near-surface flow at the wave crest has positive vorticity. Further insight into this complex flow can be gained by re-examining the flow (figure 9*c*) after subtracting an arbitrarily selected velocity from each vector. The clockwise rotation of the forward face of the wave and counter-clockwise rotation near the crest are clearly evident. Some of the observed phenomena are similar to results of experiments in a two-dimensional spilling breaker performed recently by Lin & Rockwell (1994, 1995) and Dabiri & Gharib (1997). They also observe that a shear layer starts developing at the toe of the breaker, but in their cases the shear layers extend into the liquid and do not remain attached to the forward face of the wave. The forward face and crest of their waves have very weak vorticity of opposite sign and the flows below the shear layer remain irrotational. In the present results the positive vorticity peak at the crest and below the

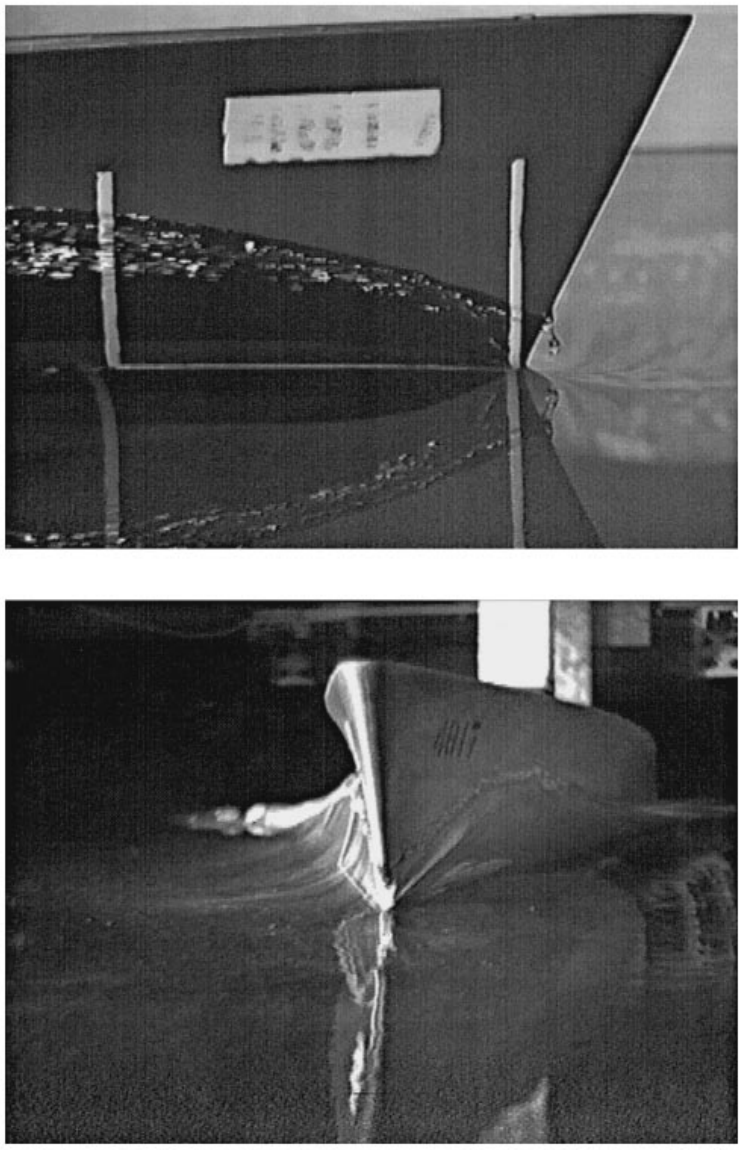

FIGURE 7. Two views of the laser sheet (film) around the bow of the ship model.

shear layer are comparable in magnitude to the peaks within the 'shear layer'. In other velocity distributions of the same flow, which were recorded in other runs (data not shown here), the exact location and magnitude of the peaks vary, but the basic pattern remains unchanged. Note that positive vorticity peaks also appear near the intersection of the free surface with the body. Like many other phenomena these peaks become much stronger and more distinct as the Froude number is increased, and will be discussed later.

The location of the present 'shear layer', along the forward face of the wave, resembles the weaker case ($Fr = 0.49$) of Lin & Rockwell's (1995) samples. However, unlike the two-dimensional cases, the vorticity-containing region in the present three-

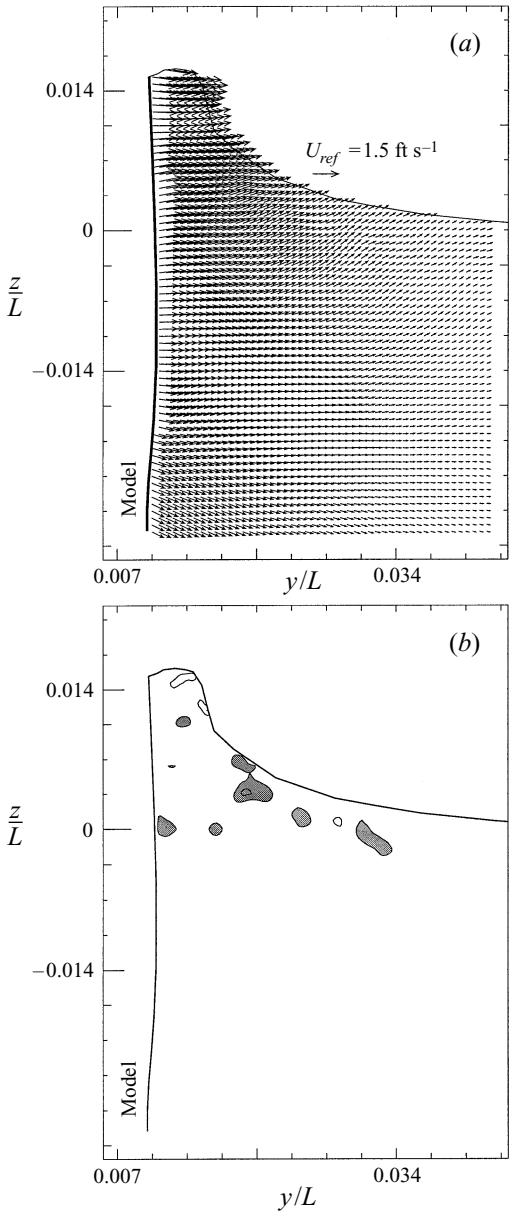

FIGURE 8. (*a*) Velocity and (*b*) vorticity ($\omega L/U$) distributions at $X/L = 0.04$ and $Fr_L = 0.279$ ($Fr_0 = 1.51$). Here and in the following figures shaded areas represent negative vorticity, and the increment between adjacent lines is 10.

dimensional wave is confined and does not have the extended shear layer that characterizes the two-dimensional cases of Lin & Rockwell (1994, 1995) and Dabiri & Gharib (1997), or the extended turbulent region behind the crest of spilling breakers discussed by Banner & Peregrine (1993). Instead, as demonstrated by photographs in figures 4 and 5 and by sample PIV data in figure 11(*b*), this vorticity is convected downstream, out of the plane of the laser sheet, in a series of vortex filaments. Thus,

the vorticity generated in the forward face of the wave in the $X/L = 0.1$ plane appears to the left (behind) the crest further downstream. For this reason, some of the vorticity appearing near the forward surface of the wave, and most certainly the negative vorticity in the flow below the crest, are generated upstream of this plane. As figure 4(*b*) also confirms, the $X/L = 0.1$ plane is located sufficiently close to the origin of the bow wave and as a result does not contain filaments to the left of the crest, but the following sections do. Other issues related to the three-dimensional flow structure within the wave are discussed in §4.

With increasing distance from the bow, at $X/L = 0.14$ (velocity in figure 10*a* and vorticity in figure 10*b*) wave breaking clearly becomes milder. Very little negative vorticity can be detected close to the toe of the wave, and positive vorticity appears near the crest. Repeated measurements to verify this trend lead to similar conclusions. However, being quite unsteady, there is considerable variation in the extent and magnitude of both the negative vorticity generated at the toe and the positive vorticity at the crest. An additional example that illustrates the extent of variability on one hand and the consistency in trends on the other is provided in figure 10(*c*). Here there is considerable positive vorticity in the wave crest and very little negative vorticity close to the toe.

As noted before, the vorticity generated at the wave crest is fed into the flow behind in a series of distinct filaments, some of which contain a single peak and others pairs of counter-rotating 'rollers'. Their locations are unsteady but they change at a low frequency enabling us to observe them in long-exposure photographs, particularly in figures 4, 5 and 6. Sample velocity and vorticity maps at $X/L = 0.2$, demonstrating the existence of such a near-surface roller pair and its effect on the surface elevation are presented in figure 11 (samples with single vorticity peaks are shown in figure 10). It is difficult to identify the origin of this specific pair in the wave crest, but based on the top-view photographs it is somewhere close to $X/L = 0.14$. This kind of free-surface deformation, caused by nearby vortical structures, has been studied experimentally by Sarpkaya & Sutton (1991) and numerically by Tryggvason (1988), Yu & Tryggvason (1990) and Dommermuth (1993). The state of knowledge on this issue is discussed in detail by Sarpkaya (1996). This pair disappears further downstream and the associated bump in the surface flattens. However, in some cases (figure 5*b*) the filaments are visible up to the crest of the following shoulder wave. Such a continuous 'shedding' of distinct vortices from the crest of the bow wave clearly distinguishes three-dimensional bow waves from two-dimensional breaking waves. At this axial location the crest of the bow wave is already located to the right of the sample area and the water elevation is decreasing everywhere. However, early signs of the next wave (typically identified as a shoulder wave) can already be identified close to the model (see also figure 4*b*). The velocity at the corner of the model and the free surface starts changing direction and new negative vorticity is already generated at the toe of the nearly forming wave. The appearance of this wave becomes more obvious further downstream, at $X/L = 0.27$ (figure 12), as the flow near the body turns upward, the negative vorticity peak at the toe is clearly evident and the surface elevation to the right of the toe is still decreasing. Note that all the velocity in this plane is very low (scales are different than previous figures), in the order of 5% of the ship speed, and the data are limited to regions where the displacement between exposures is sufficient to provide reliable data (no overlap between particle traces). At higher X/L the velocity is even lower and the region of resolved flow is even more limited. These data do not provide additional significant information.

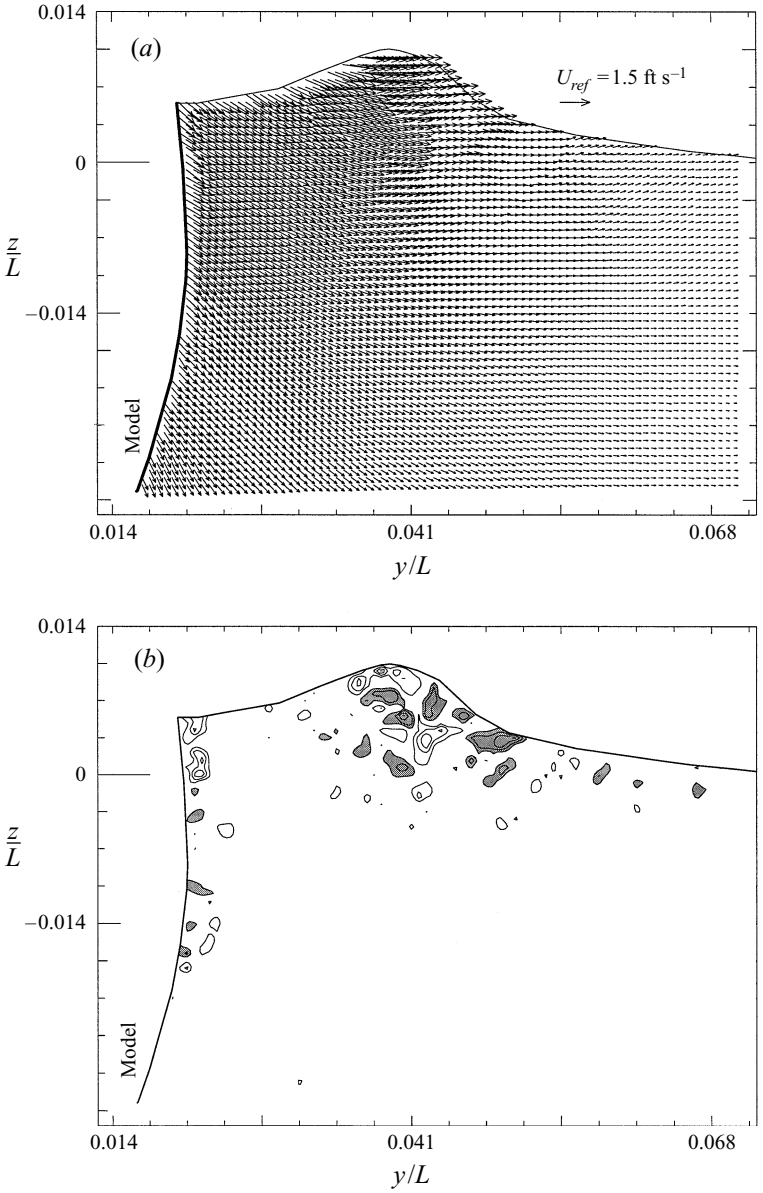

FIGURE 9(*a*, *b*). For caption see facing page.

3.3. *Bow wave with a steep slope*

Four sample cross-planes, which were recorded during the same experiment and whose locations are marked on figure 6(*b*), are provided for $Fr_L = 0.446$. The first two planes (figures 13 and 14) are located within the liquid sheet upstream of the main bow wave. At $X/L = 0.01$ (figure 13) the upper portion of the film is very thin (only 2 mm at $z/L = 0.0169$) and it ends in a sharp tip. As noted before, the tip of this film frequently rolls up as the liquid loses its momentum, but that portion of the flow cannot be seen from below. Owing to this momentum loss close to the top of the sheet the vectors are inclined upward only slightly, and their magnitudes are only about 14% of the ship speed. Below the tip the flow turns upward and increases to about 20%. The vertical

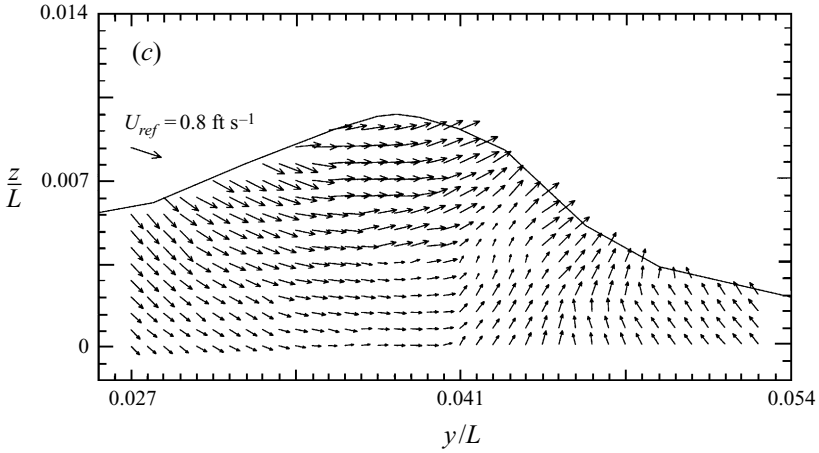

FIGURE 9. (*a*) Velocity and (*b*) vorticity ($\omega L/U$) distributions at $X/L = 0.10$ and $Fr_L = 0.279$. (*c*) Magnified portion of the velocity field after subtracting a constant reference velocity (identified as U_{ref}).

component of the velocity near the body gradually decreases and changes direction near $z/L = -0.0135$, the same height as the mild wave. Thus, again, close to this location the flow in a vertical plane has a saddle (attachment) point. The liquid below moves towards the bottom of the ship and the liquid above is involved in the wave motion. Further away from the body the upward trend extends to a larger depth. One may choose to use this observation to replace the draught with $0.40D$ or $0.0135L$ as the proper length scale for calculating the local Froude number. Interestingly, the thickness of this layer in the present mild slope case (figure 8) is also $0.0135L$, i.e. this length scale does not seem to depend on the Froude number. However, more research is needed in order to determine the relationship between the draught, hull geometry and the thickness of the layer involved with wave motion before drawing conclusions.

Even at this location the liquid sheet already contains a considerable number of vorticity peaks (figure 13*b*). Near the tip most of the peaks are positive, but lower down the vorticity becomes predominantly negative and the flow seems to have a diagonal structure with vorticity trains of alternating signs. Since boundary-layer-produced vorticity in this region of upward flow should be positive, the negative peaks must be generated at the free surface. As discussed by Longuet-Higgins (1994), a curved free surface with velocity component parallel to it, as in the present case (a detailed discussion will follow), must contain near-surface vorticity. Owing to the upward flow direction and the concave free surface, this vorticity should be negative, in agreement with the experimental data. This agreement does not explain the mechanism causing transport of this vorticity away from the surface, which will be discussed later. At this point we also do not have a well-founded explanation for the formation of what appears to be penetrating 'shear layers' of alternating signs. Finally, although the boundary layer can be responsible for the positive peaks near the top of the sheet, their centres, especially the lower one, are also located near the free surface. This trend becomes clearer further downstream and will be discussed as the results are presented.

At $X/L = 0.08$ (figure 14), the flow near the crest of the liquid sheet, whose thickness is about 1% of the body length (and a third of the draught), is already starting to turn downward. At this location the sheet is close to its maximum elevation which,

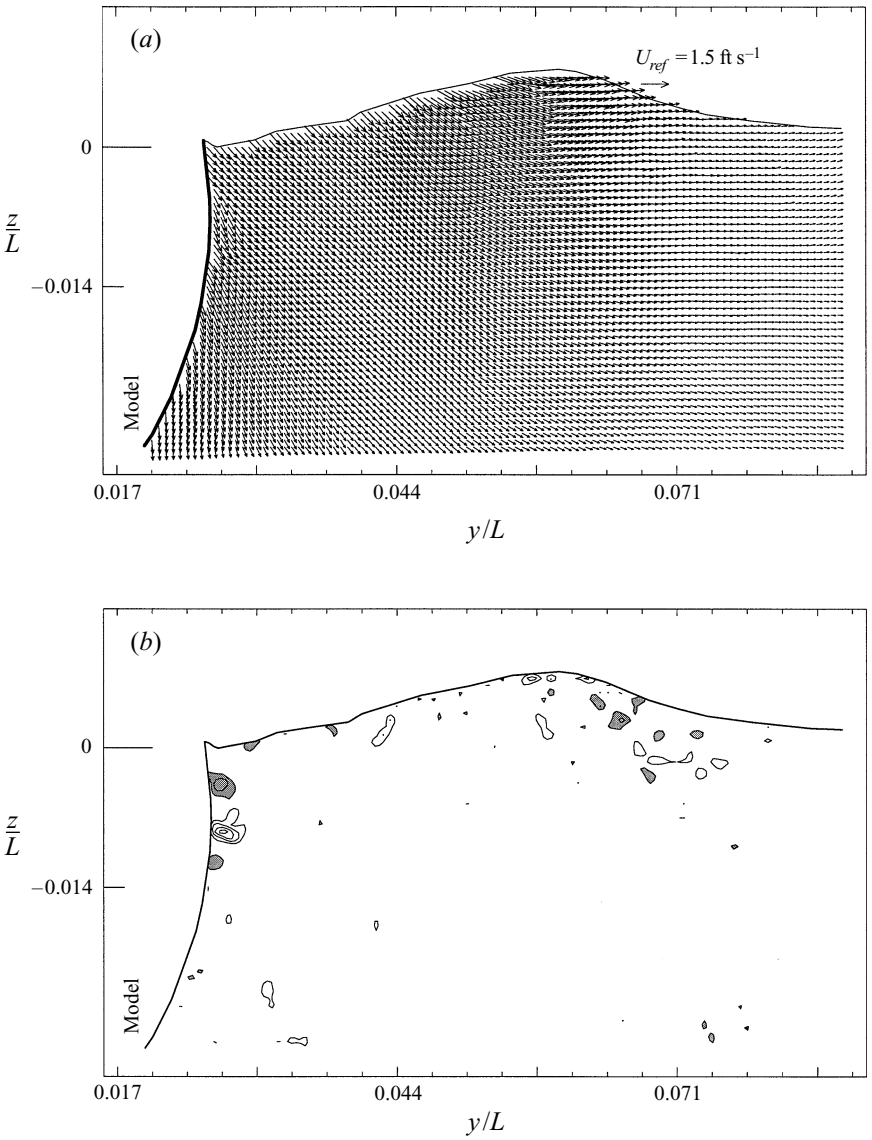

FIGURE 10(*a*, *b*). For caption see facing page.

accounting for the orientation of the illuminated plane, is about 1.6% of the ship length and 48% of the draught. Although the sheet contains both positive and negative vorticity peaks (figure 14*b*), the positive peaks are clearly dominant. As noted before, positive vorticity can be generated both in the boundary layer on the surface of the model (due to the upward motion and inclination of the light sheet) and on the free surface, due to the surface curvature and existence of a velocity component parallel to it. Careful examination of this flow, augmented with a vector map that shows the same flow after subtracting an arbitrarily selected constant velocity from each vector (figure 14*c*) reveals quite a complex structure. Close to the wall and the tip of the liquid sheet the flow turns downward after losing its momentum, presumably due to wall stresses. This downward trend stops quite abruptly at $z/L \sim 0.0203$ in a region of high vorticity.

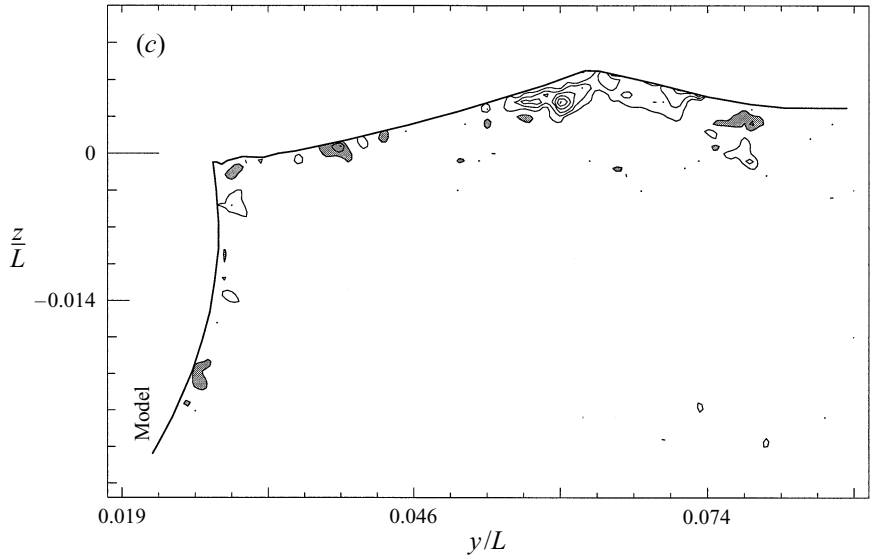

FIGURE 10. (*a*) Velocity and (*b*) vorticity ($\omega L/U$) distributions at $X/L = 0.14$ and $Fr_L = 0.279$. (*c*) Additional vorticity distribution from a different run (at $X/L = 0.16$ and $Fr_L = 0.279$), demonstrating the variability in the flow structure.

This change seems to indicate that boundary layer separation, which feeds the boundary layer vorticity away from the surface, occurs at this location. This separation is particularly clear in the reference frame of figure 14(*c*). There are also several additional positive vorticity peaks along the outer, free-surface side of the sheet, whose existence and sign is consistent with the surface curvature and direction of the velocity component parallel to the surface (in the ship frame of reference for which the mean flow is steady). The mechanism causing transport of this vorticity away from the surface is a separate issue, which will be discussed in §4. As will be demonstrated shortly (figures 15 and 16) the vorticity structure within the sheet has a significant impact on the flow near the surface of the model far downstream of the bow wave.

Another obvious phenomenon at $X/L = 0.08$ is the abrupt change in surface slope at $y/L = 0.0302$, which marks the intersection of the liquid sheet with the forward face of the main bow wave. A layer of turbulent flow with weak vorticity peaks of both signs, but with significantly more negative peaks, starts close to this point and extends into the liquid away from the surface. A similar phenomenon appears also in the milder Froude number case (figure 8*b*), where the vorticity train is more continuous and almost always negative. Although the vorticity is weak the existence of the turbulent layer suggests that the flow separates and forms a shear layer, whose origin is at the free surface, at the intersection between the sheet and the bow wave. The weak vorticity within this turbulent layer, especially in the high Froude number case, may be a result of the orientation of the laser sheet relatively to the vorticity vector. The magnified vector map (figure 14*c*) clearly shows the abrupt change in flow direction close to the toe of the sheet. With the correct perspective, this phenomenon is not different in principle from the formation of a shear layer near the toe of the spilling breaker (figure 9 and Lin & Rockwell 1994, 1995; Dabiri & Gharib 1997). Also evident is the formation of a pair of counter-rotating vorticity structures near the model at $z/L \approx 0$ (the far-field water elevation). Traces of a similar pair also appear at $X/L = 0.01$ (figure 13*b*), suggesting that it is originated at the bow of the ship.

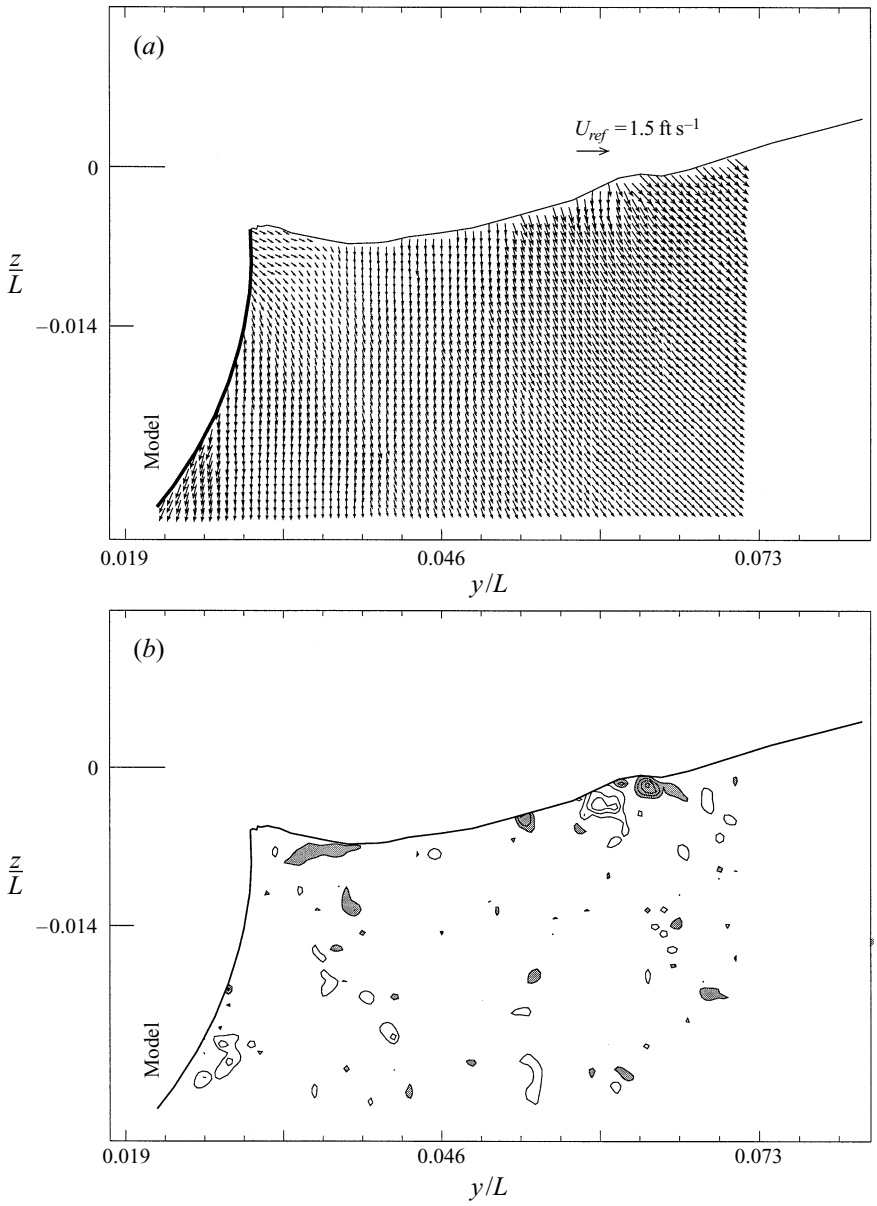

FIGURE 11. (*a*) Velocity and (*b*) vorticity ($\omega L/U$) distributions at $X/L = 0.20$ and $Fr_L = 0.279$.

Further downstream, at $X/L = 0.15$ (figure 15), there are two distinct phenomena. The first is the flow structure within the bow wave, and the second is the flow near the body. Although the entire flow structure is unsteady, the observed trends and structures are quite repeatable and can be seen in other images in the same plane. The forward face of the bow wave is quite steep, and in fact, a short distance further away from the model, close to $X/L = 0.2$, it actually plunges to create a bubbly wake, as can be clearly seen in figure 6(*b*). The magnitude of the velocity within almost the entire wave crest exceeds 20% of the ship speed, a level which is significantly higher than in any region in the surrounding flow. The velocity drops quite abruptly to less than 8% near the toe of the wave ($y/L = 0.06049$), and then increases slightly again to 8–10%

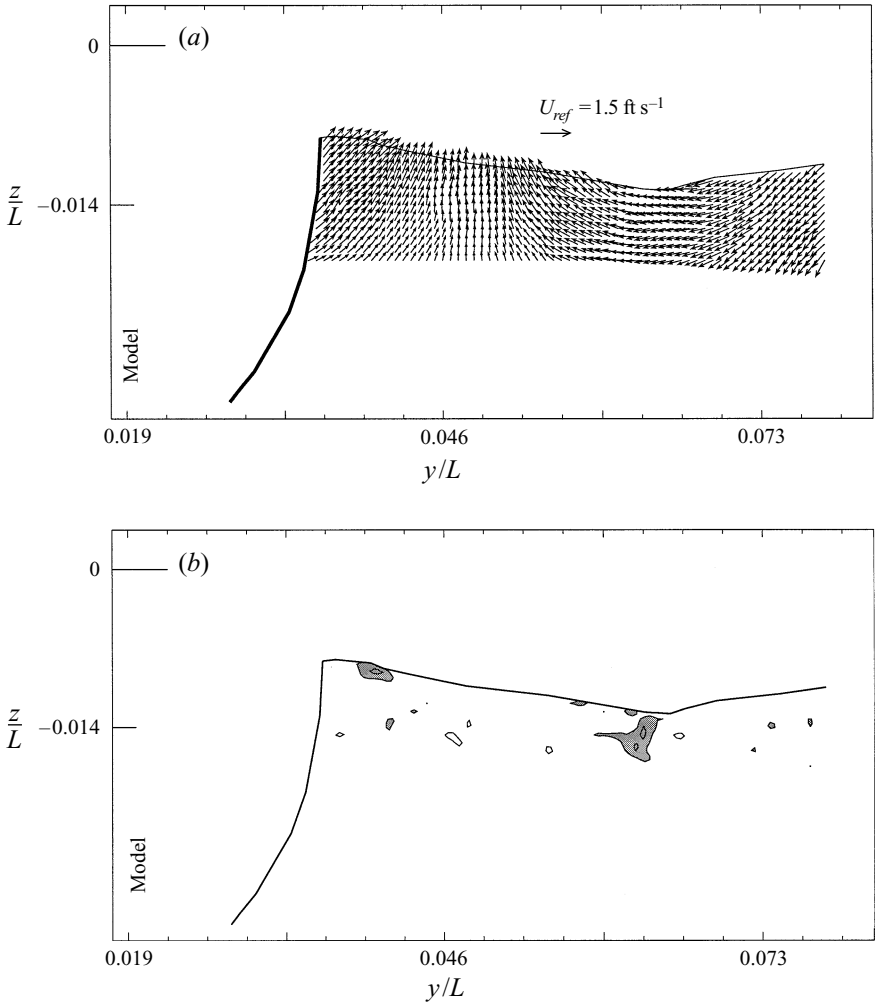

FIGURE 12. (*a*) Velocity and (*b*) vorticity ($\omega L/U$) distributions at $X/L = 0.27$ and $Fr_L = 0.279$.

for the rest of the near-surface region. The extent of this abrupt change is highlighted in figure 15(*c*), which shows the same flow after subtracting an arbitrarily chosen vector from each image. This abrupt change is consistent with Miyata & Inui's (1984) claim that the flow within a bow wave bears some analogy to an oblique shock wave, namely the velocity component normal to the wave crest decreases at the 'shock', causing a sudden change in flow direction. The change in velocity is more gradual to the left of the crest. It decreases from 20% at $y/L = 0.0503$ to 18% at $y/L = 0.0436$, 14% at 0.0348 and 12% at 0.030 before starting to increase very close to the model.

The vorticity within the wave (figure 15*b*) is predominantly negative and its origin seems to be located at the toe of the wave, where the surface slope changes abruptly. This observation is consistent with the mild bow wave case (figure 9) and previously mentioned recent measurements in two-dimensional spilling breakers (Lin & Rockwell 1994, 1995; Dabiri & Gharib 1997). However, unlike the two-dimensional cases, for which a horizontal shear layer forms, the negative vorticity wraps around a small positive peak and returns back to the forward face of the wave. This trend, namely that most of the negative vorticity remains concentrated in the forward portion of the wave,

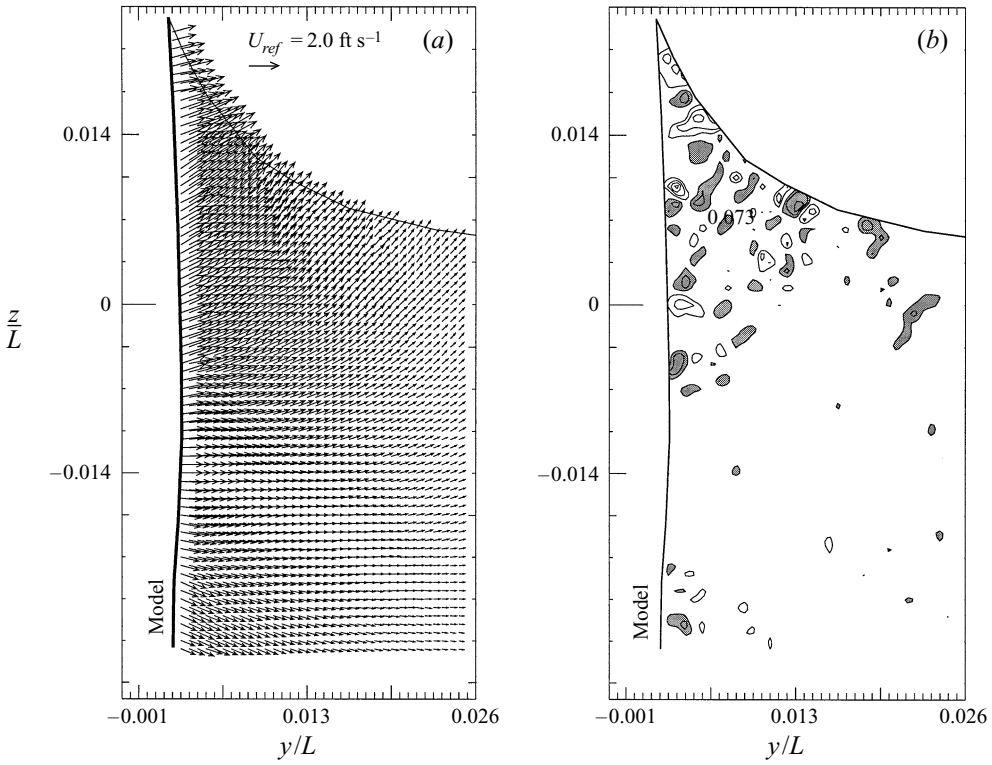

FIGURE 13. (*a*) Velocity and (*b*) vorticity ($\omega L/U$) distributions at $X/L = 0.01$ and $Fr_L = 0.446$ ($Fr_D = 2.41$).

is consistent with the present mild case. Also similar are the extensions of the negative vorticity into the flow below the wave crest, and the powerful counter-rotating peak near the highest point of the wave. This latter phenomenon is very weak in two-dimensional wave (Lin & Rockwell and Dabiri & Gharib). Thus, in spite of the differences in wave-front shapes and Froude numbers, the vorticity distributions within the mild and steep bow waves, close to their origins, have a lot in common. Both contain mostly negative vorticity, especially in their front surfaces, but they have powerful counter-rotating vorticity peaks close to the wave crest. In both cases this vorticity is fed into the flow downstream in a series of clearly defined filaments. The positive peaks and the formation of filaments (three-dimensional effects) clearly distinguish the bow waves from classical models describing spilling breakers as enclosed regions containing negative vorticity (for the present coordinate system and flow direction), as discussed in detail by Banner & Peregrine (1993). The presence of numerous vortex structures, whose locations and strengths are unsteady, is consistent with Peregrine & Svendsen's (1978) perception, as described also in Banner & Peregrine's (1993), that a spilling breaker toe is the origin of a turbulent region. The possible existence of such counter-rotating flows near a free surface and the resulting local dividing streamlines, attachment and separation points have been predicted, based on theoretical arguments, by Lugt (1987). Section 4.2 in this paper, which deals with vorticity production along the surface of the bow wave, explains the origin of the positive vorticity at the wave crest and the negative vorticity at the toe.

The second major phenomenon, which is evident at $X/L = 0.15$, is the high velocity, at spots as high as 20% of the ship speed, and associated regions with positive vorticity near the surface of the ship. The same phenomenon also appears at $X/L = 0.24$, but at a greater distance from the free surface (figure 16). Reasons for this trend will be discussed shortly. Furthermore, although less obvious, a milder case of the same trend also appears near the body at $Fr_L = 0.279$ (figure 9) and can be detected near the model even at $X/L = 0.20$ (figure 11). The origin of this high-positive-vorticity flow can be traced to the tip of the liquid sheet upstream of the bow wave (figure 14). As discussed before, this vorticity is generated in part on the free surface (a more detailed explanation is provided in the next section) and in part on the solid boundaries during upward motion of the liquid sheet, from which it is convected due to boundary layer separation. This vorticity-rich fluid remains close to the model even downstream of the bow wave. However, a comparison of the data at $X/L = 0.15$ and $X/L = 0.24$ shows a slight detachment of the fluid with positive vorticity from the body, and formation of a growing region with negative vorticity below the positive region (below $z/L = -0.0081$ in figure 15(*b*) and -0.02166 in figure 16*b*). Some negative vorticity also starts appearing at $X/L = 0.24$ between the positive bulk and the wall. Generation of negative vorticity is consistent with the direction of flow near the body in the vicinity of the positive vorticity region (see an example of the flow relatively to the body in figure 17) and its detachment from the boundary can be explained as secondary motion induced by the high positive vorticity above it. In the right coordinate system (not shown here) the flow in this region appears as a pair of unequal vortices of opposite signs. Thus, vorticity structures associated with formation of the liquid sheet and the bow wave affect the flow near the surface of the body well downstream of the bow wave. To the best of our knowledge, existence of this phenomenon has not been reported before. Further downstream (data not shown), the effect of the liquid sheet on the vorticity distribution near the body slowly diminishes. Near mid-ship all the velocity within the illuminated plane decreases to less than 4% of the ship speed and becomes difficult to resolve with multi-exposure PIV (without image shifting, which will be used in future studies).

One of the trends that has to be explained is the increasing distance between the fluid with positive vorticity and the free surface. Note that in figure 15(*a*) the flow near the body is directed away from its boundary and in figure 16 the trend is mostly downward. However, these directions are a result of presenting data in a stationary frame of reference, which is inclined as shown in figure 1. A downward velocity in this plane means that there is actually flow towards the body near the intersection of the free surface with the model (i.e. in figure 16 we are beyond the trough and the water level is already rising). The influx towards the body brings external fluid that was not part of the original sheet, which increases the distance of the bulk with positive vorticity from the surface.

4. Discussion and analysis

4.1. *Three-dimensional effects*

As noted before, the three-dimensional structure of the bow wave becomes evident by simply comparing the velocity and vorticity distributions in successive close planes. However, additional significant trends can be identified by carefully re-examining the data. For example, if we project the present data and wave shape onto a vertical plane,

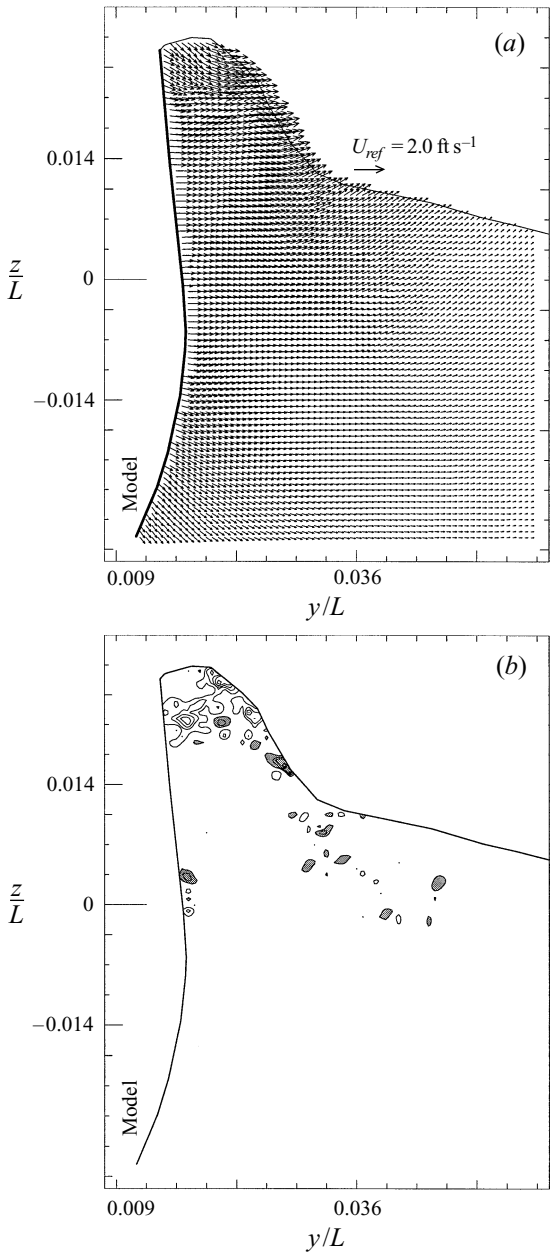

FIGURE 14(*a*, *b*). For caption see facing page.

identified as the (y', z')-plane in figure 1, the velocity normal to the surface, $u_{n'}$, should be very small if the flow is steady and if changes in surface elevation in the x'-direction (parallel to the wave crest) are small. The latter assumption will be verified later. Assuming that $u_{n'} = 0$ then

$$w' = -v' \tan \beta', \tag{1}$$

where

$$\beta' = -\tan^{-1}[\cos 38^\circ (\partial z/\partial y)|_{surface}] \tag{2}$$

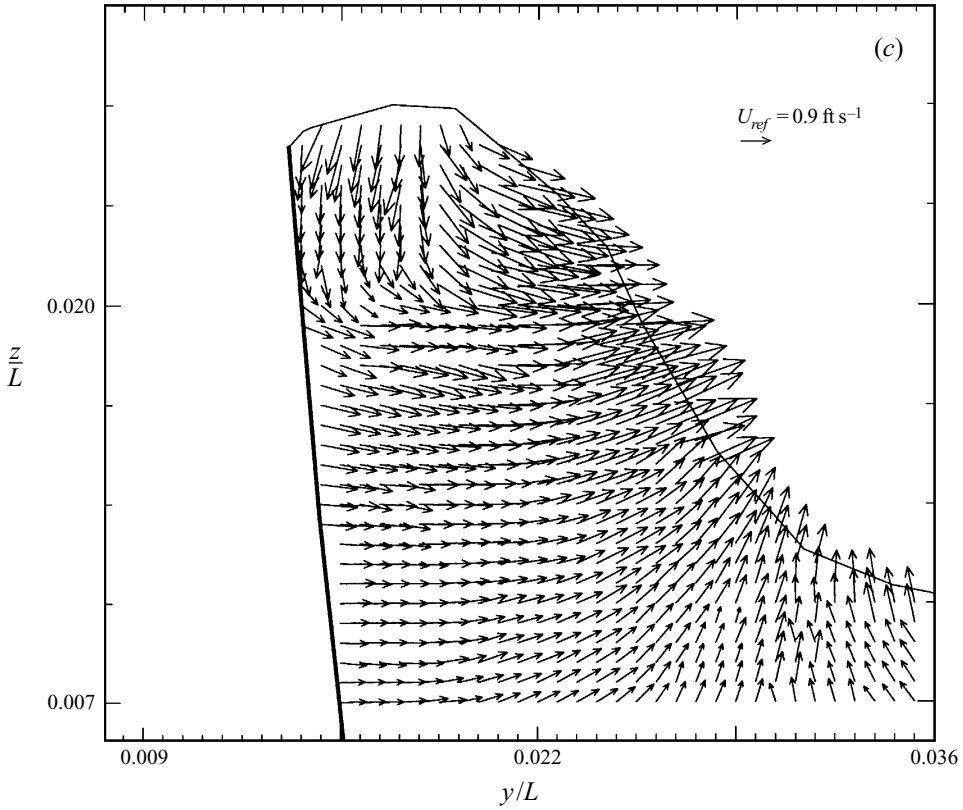

FIGURE 14. (*a*) Velocity and (*b*) vorticity ($\omega L/U$) distributions at $X/L = 0.08$ and $Fr_L = 0.446$. (*c*) Magnified portion of the velocity field after subtracting a constant reference velocity (identified as U_{ref}).

is the slope of the free surface. Since

$$w = u' \sin 38° + w' \cos 38° \tag{3}$$

then

$$u' = \frac{w}{\sin 38°} - \frac{w'}{\tan 38°} = \frac{w}{\sin 38°} + \frac{v' \tan \beta'}{\tan 38°}, \tag{4}$$

$$u_{s'} = v'/\cos \beta', \tag{5}$$

where $u_{s'}$ is the velocity component tangent to the free surface. Thus, noting that $v' = v$, it is possible to compute all three components of the velocity along the free surface. The resulting surface distributions of these components at $X/L = 0.1$ are plotted in figure 18, along with the total velocity and total energy. The latter is the sum of the kinetic energy and surface elevation scaled with the total head, based on the ship speed, $U^2/2g$. All the data are in the ship frame of reference. The magnitude of the total velocity and head on the right-hand side confirm that the error caused by assuming that $u_{n'} = 0$ is small. As is evident from the result the velocity parallel to the wave crest, u'/U, first decreases along the forward face of the wave, reaching a minimum value at

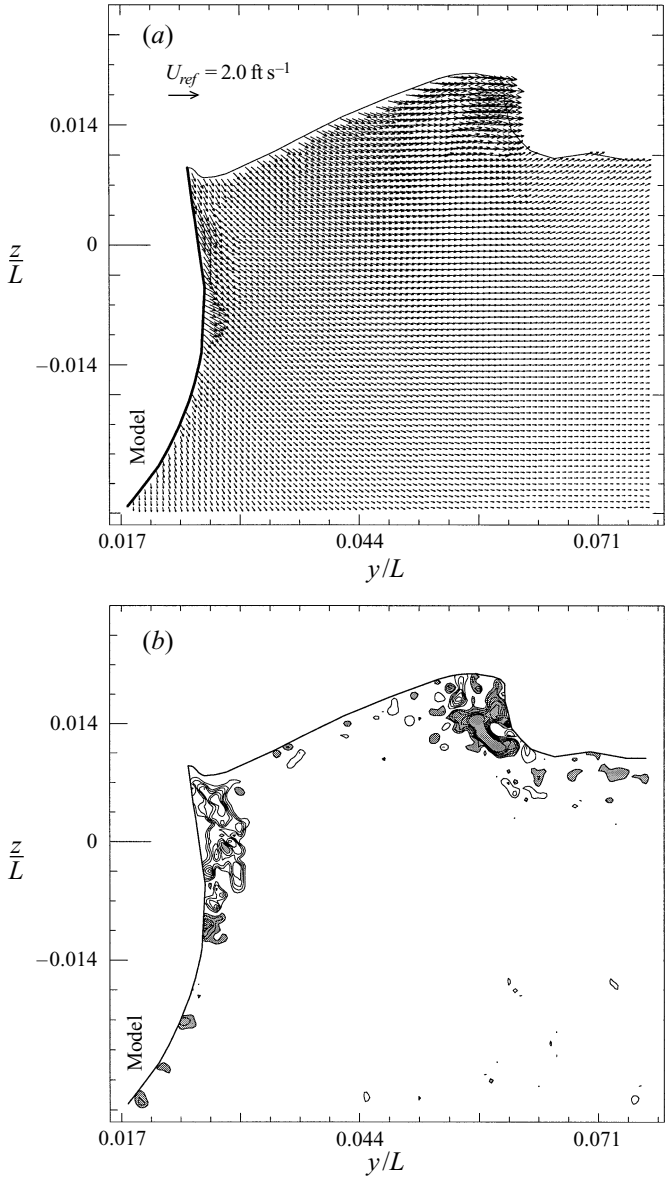

FIGURE 15(*a*, *b*). For caption see facing page.

$y/L = 0.046$, i.e. in the middle of the forward face. It then increases near the crest and decreases again between the crest and the model. These trends are consistent with measurements around a towed 20° wedge, performed below the surface with a Pitot tube, which are discussed in detail by Miyata & Inui (1984). Trends in the vertical velocity are also consistent. Thus, the assumption that $u_{n'} = 0$ leads to the correct trends. Miyata & Inui's data on head losses show considerable reduction in total head between the forward face of the wave and slightly upstream of the crest, as in the present results, followed by recovery to almost the initial total head behind the wave crest, also in agreement with the present data. According to the present results the total

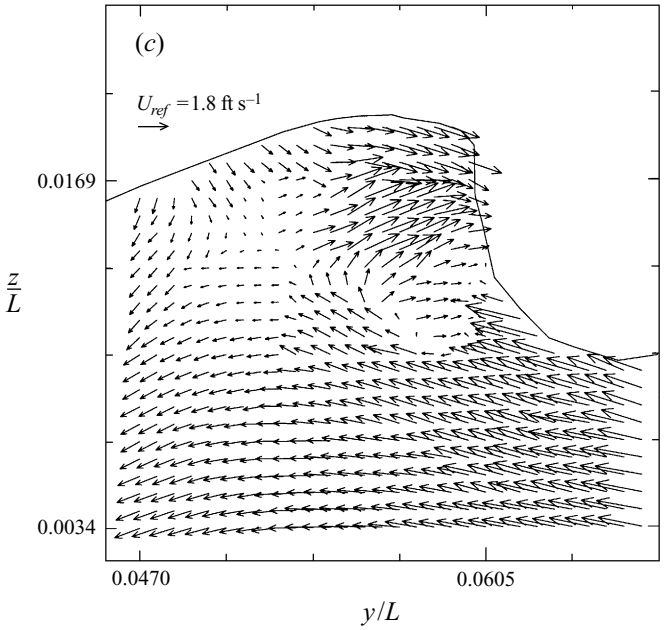

FIGURE 15. (*a*) Velocity and (*b*) vorticity ($\omega L/U$) distributions at $X/L = 0.15$ and $Fr_L = 0.446$. (*c*) Magnified portion of the velocity field after subtracting a constant reference velocity (identified as U_{ref}).

head decreases again substantially between the wave crest and the body. Such a trend is not observed in Miyata & Inui's data. The discrepancy may be in part a result of operating at different Froude numbers (theirs is 1.1 and ours is 1.5, both based on the draught), which means substantial differences in the near-surface turbulence. However, it is more likely that the primary difference is that the present measurements are performed 'on the surface' (the interrogation window is about 3.2 mm wide) and their data are limited to more than 1 cm below the surface. As they also noted, and the present results confirm, most of the dissipation away from the wave crest and near the body is confined to a fairly thin layer close to the free surface.

The present trends suggest that within the wave the maximum dissipation occurs near the toe, where the flow apparently separates, and loss of energy occurs over the entire forward face of the mild wave (prior to plunging), where the vorticity is negative (figure 9). Miyata & Inui's results confirm that this trend is not limited to the present model and Froude numbers. There is very little dissipation to the left of the wave crest, where the vorticity is positive, at least in the mild wave case. One still has to explain how the fluid behind the crest has a total head that is higher than the head in the forward face. Miyata & Inui suggest that the recovery to the initial energy level occurs due to mixing with fluid whose energy is much less dissipated. Since there is no room or evidence for such mixing so close to the origin of the bow wave (see the location of this section in figure 4), it is more likely that for the present case the fluid just behind the crest at $X/L = 0.1$ passes through the forward face of the wave at an upstream point where there is little dissipation. For example, at $X/L = 0.04$ (figure 8) the entrained vorticity in the forward face is minimal, suggesting that the dissiption there

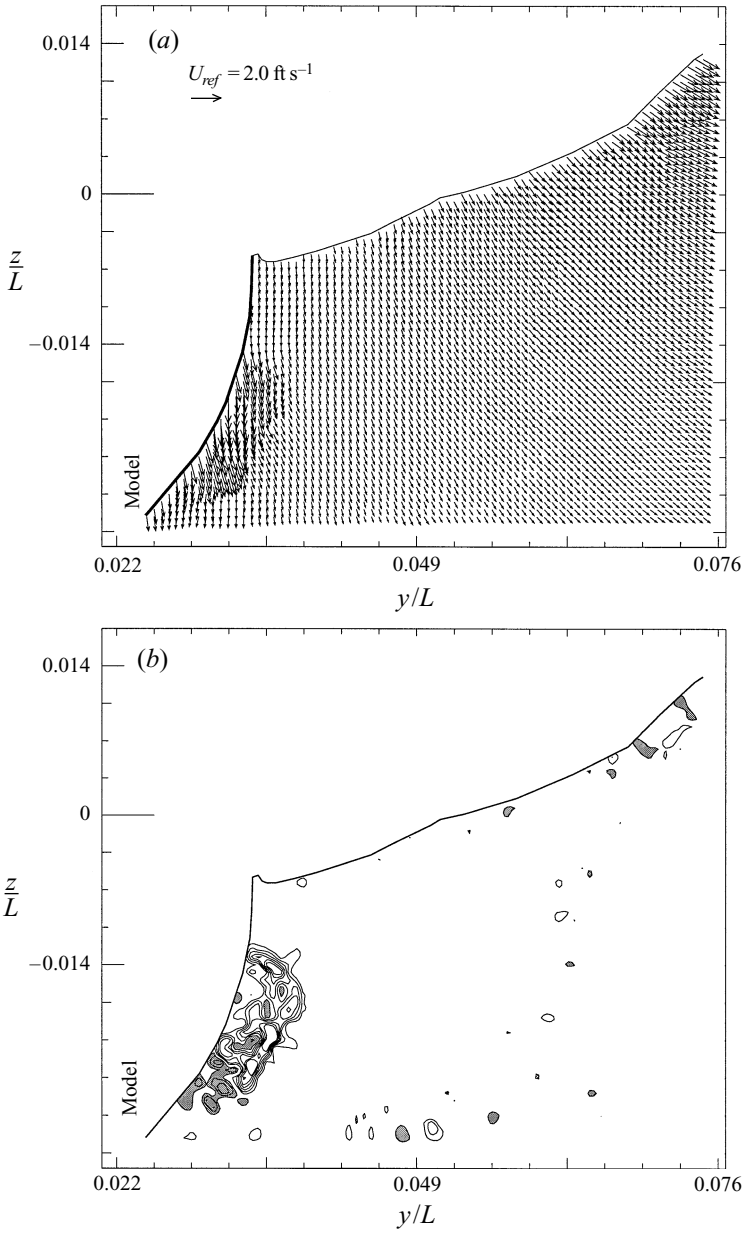

FIGURE 16. (*a*) Velocity and (*b*) vorticity ($\omega L/U$) distributions at $X/L = 0.24$ and $Fr_L = 0.446$.

is smaller. Behind the energy peak, namely at $y/L < 0.0234$, the total head decreases again all the way to the model, presumably due to the effect of dissipation within the liquid sheet.

At $X/L = 0.14$ (figure 19) the dissipation along the forward face is smaller, consistent with the weaker breaking in this plane. However, there is only a slight trace of total head recovery near and behind the crest, followed by further decrease. Being sufficiently downstream of the origin of the wave, the data suggest that all the (near-surface) fluid passes through the breaking region and as a result substantial energy loss occurs everywhere. The total head continues to decrease behind the crest until

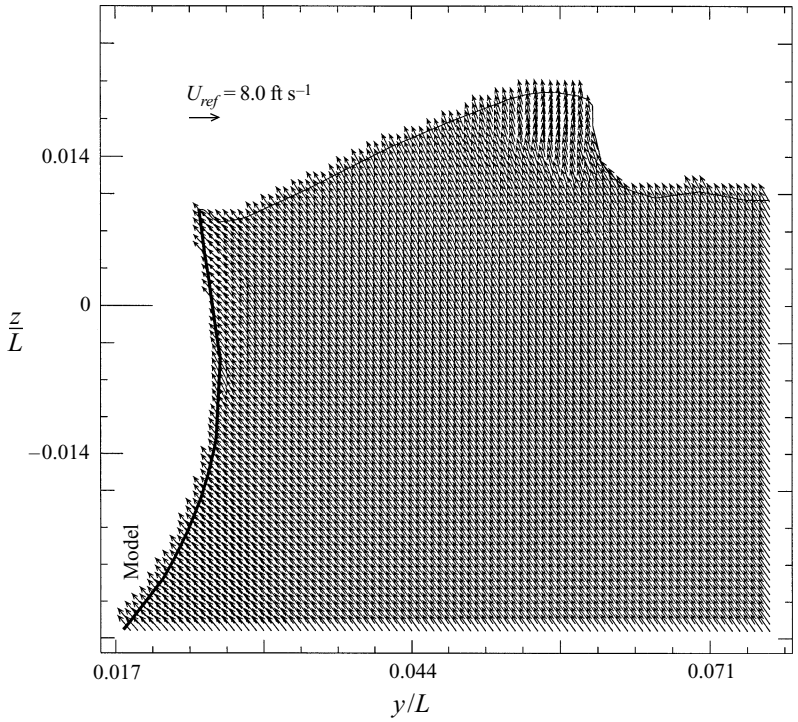

FIGURE 17. Velocity field at $X/L = 0.15$ and $Fr_L = 0.446$ in the ship frame of reference, i.e. after subtracting the projection of the ship velocity on the illuminated plane.

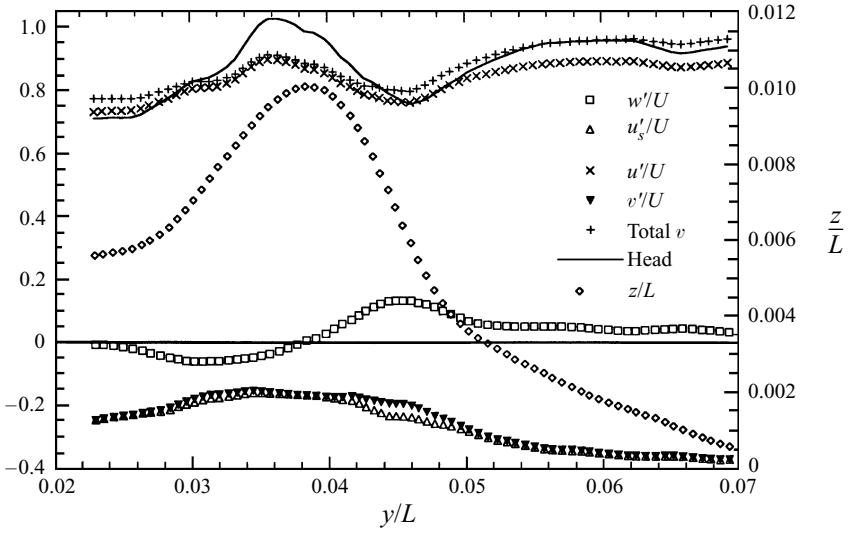

FIGURE 18. Distributions of all three components of the velocity, the total speed and the total head along the free surface at $X/L = 0.10$ and $Fr_L = 0.279$. The data are presented in the ship frame of reference and the corresponding coordinates (x', y', z') are defined in figure 1(*b*). The velocity is determined using the experimental data and by assuming that $u_{n'} = 0$.

$y/L = 0.04$ to a minimum of ~ 0.68, followed by recovery to a maximum of 0.75 at $y/L = 0.034$ and further decrease to 0.62 near the model. One can speculate on the origin of this local maximum, but it is of no great significance (for the purpose of this paper)

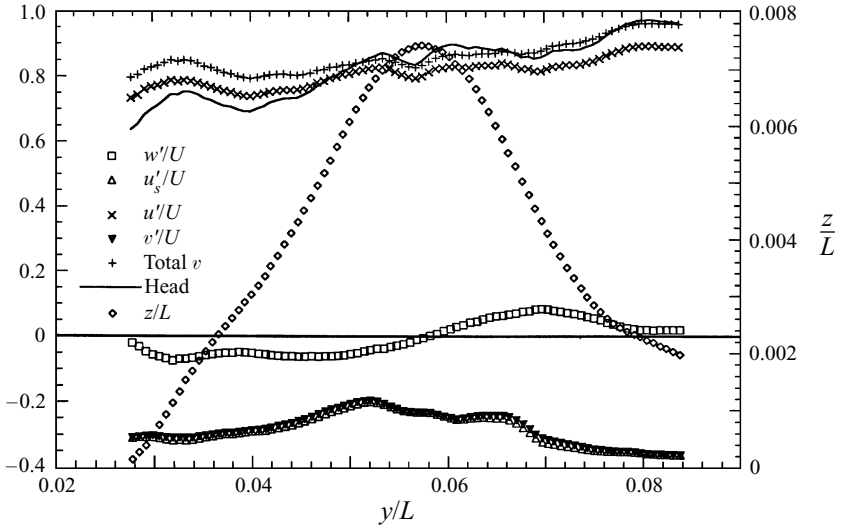

FIGURE 19. As figure 18 but at $X/L = 0.14$ and $Fr_L = 0.279$.

since it is located between the bow and the origin of the shoulder wave. It may be a residual of the maximum on the wave crest at $X/L = 0.1$, which occurs at almost the same distance from the model centre ($y/L = 0.036$ vs. 0.034), or another portion of fluid that crosses the crest in a less dissipative region of the wave. The steeper decrease near the model, caused mainly by a sharp decrease in u'/U, is probably associated with early signs of the formation of the shoulder wave. As shown in figure 4(*b*), the $X/L = 0.14$ laser sheet intersects with the model close to the origin of the shoulder wave.

Another related phenomenon of interest is the change in flow direction, $\Delta\alpha$, caused by the wave, which can be estimated from

$$\Delta\alpha = \tan^{-1}(v'/u') + 25°. \tag{6}$$

Results for $X/L = 0.1$ and 0.14 are presented in figure 20(*a*) and 20(*b*), respectively. The initial angular shift, 2.1°, occurs in part since the flow is already slightly turned outward on the right-hand side of the vector map, but may also be affected by error associated with our assumption that $u_{n'} = 0$. In any case it is very small. At $X/L = 0.1$ the direction changes gradually to more than 15° beyond the wave crest and then gradually decreases, but only to 6°. At $X/L = 0.14$ the changes are abrupt, both as the angle increases along the wave front, and when the angle decreases back. The maximum angular shift is only 12°, but the flow angle returns to 2.2°, very close to the model. Considering that the model half-expansion angle at this location is about 6.5°, then the flow near the model at $X/L = 0.1$ matches this angle quite well, but there is a clear angular mismatch at $X/L = 0.14$. Such a mismatch would lead to flow 'impingement' on the surface, which triggers the formation of the shoulder wave. Further downstream, as the top view photographs in figures 4 and 5 clearly show, the flow between the bow and shoulder waves turns even further towards the model and $\Delta\alpha$ actually becomes negative.

The fairly abrupt change in velocity and flow direction within the wave have led Miyata & Inui to claim that the bow wave is analogous to an oblique shock, across which the tangential velocity component, u' in the present case, remains unchanged,

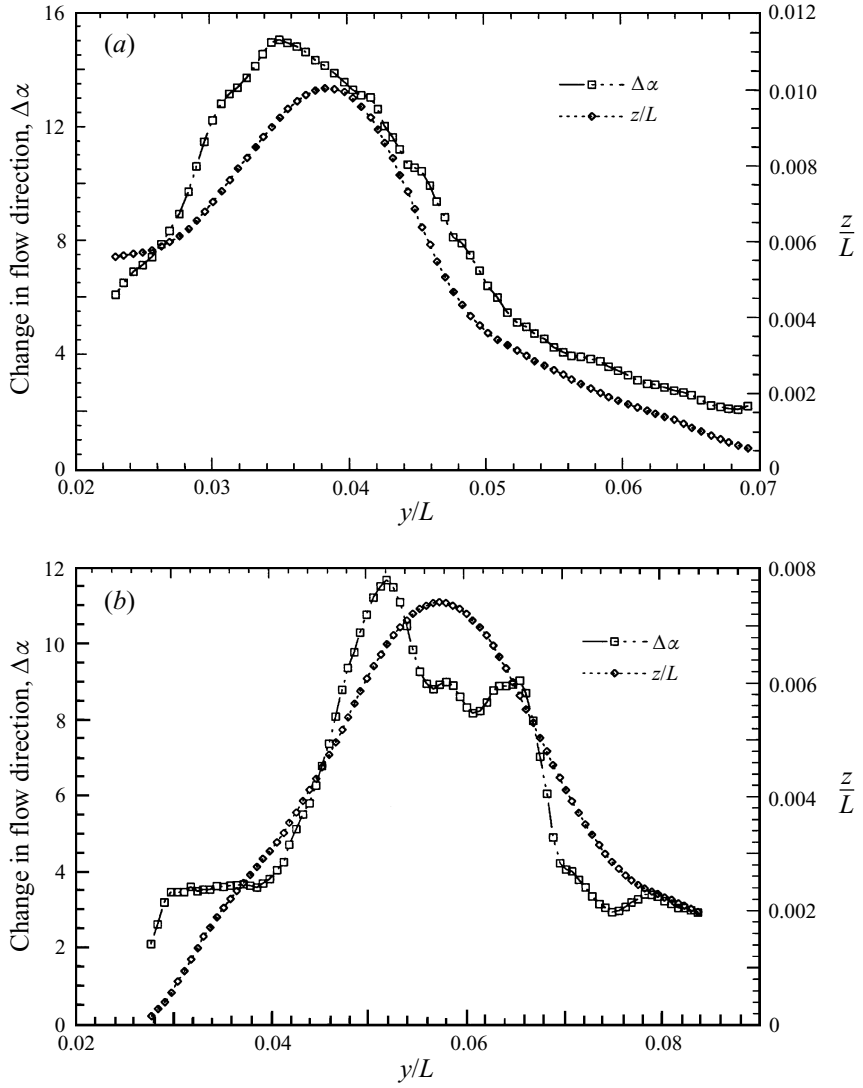

FIGURE 20. Change in flow direction (in degrees) along the surface at (*a*) $X/L = 0.10$ and (*b*) $X/L = 0.14$, both at $Fr_L = 0.279$.

whereas the normal component, v', decreases. They also provide data to support this argument. In the present flow near the surface at $X/L = 0.1$ both and v' and u' change significantly across the wave. At $X/L = 0.14$ the decrease in u' within the wave is considerably smaller, between 0.88 to 0.78, while v' first decreases substantially, from -0.36 to -0.2, but then it increases again to -0.3. Thus, there is a somewhat better agreement with the shock analogy.

A question that will become an issue in the next section is the relative magnitude of 'crest-wise' gradients ($\partial/\partial x'$) of variables in comparison to the gradients in the cross-planes $\partial/\partial y'$ and $\partial/\partial z'$. In order to provide an order of magnitude estimate using the present data, we use the velocity and elevation distributions at $X/L = 0.1$ and 0.14 that are recorded during the same experiment. Graphical comparisons of 'wave height' (recall that the actual height is $0.788z/L$) and $v'/U = v/U$ on the surface are presented in figure 21(*a*). Note that the y/L coordinate of the data at $X/L = 0.14$ is shifted to

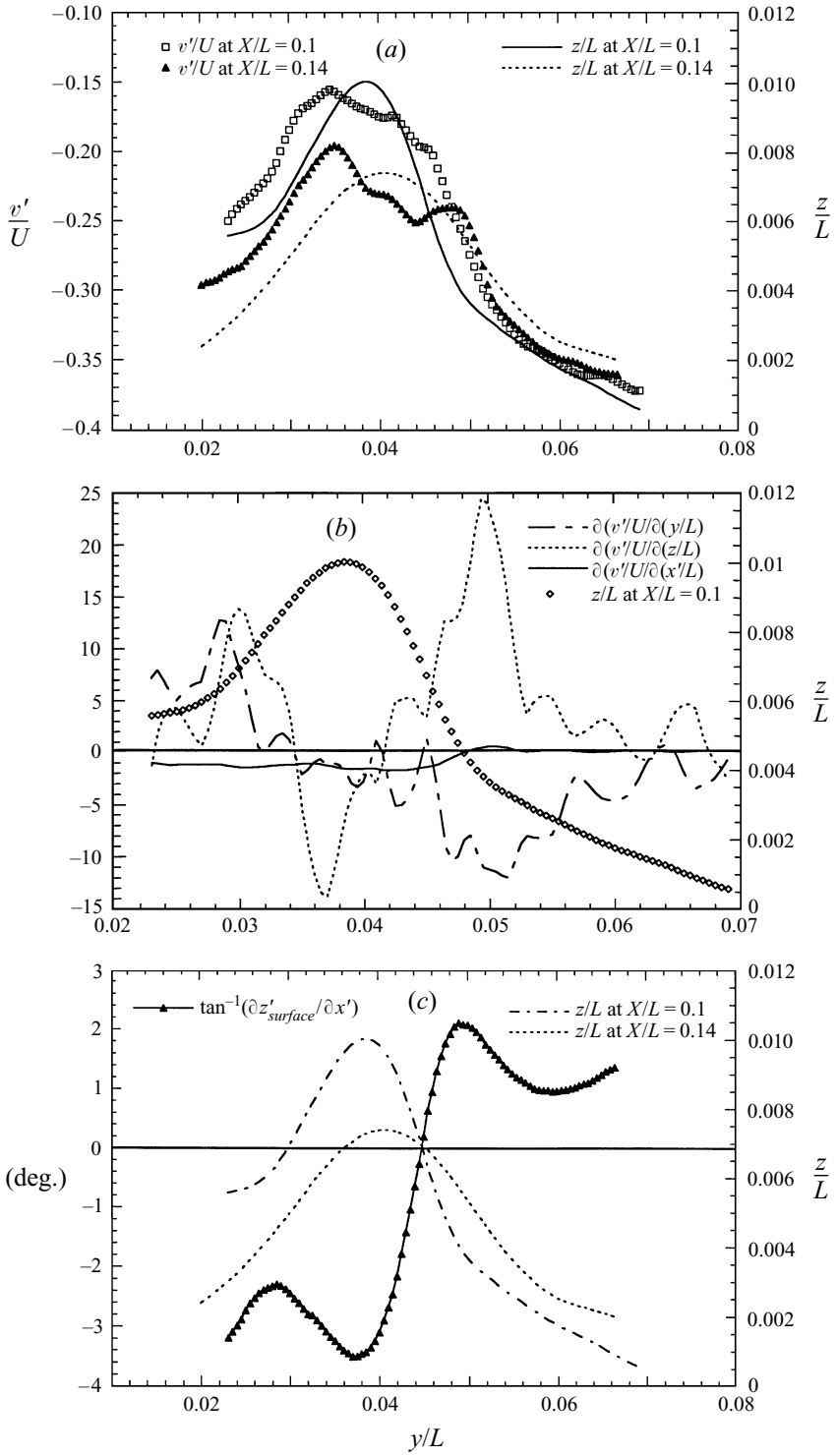

FIGURE 21. (*a*) Variations in the wave cross-section and v'/U ($v' = v$) along the surface at $Fr_L = 0.279$. (*b*) A comparison between the characteristic velocity gradients along the surface within the laser sheet ($\partial/\partial z$ and $\partial/\partial y$) to the gradients in the x' (parallel to the wave crest) direction. (*c*) The surface slope in the x'-direction between $X/L = 0.10$ and 0.14 at $Fr_L = 0.279$.

match that corresponding coordinates at $X/L = 0.1$. It is evident that the wave height decreases and its width increases with increasing distance from the model. The values of v'/U are almost identical along the lower, forward face of the wave, but they are different near and behind the wave crest. The estimated gradients are compared in figure 21(*b*). Based on these estimates it is clear that $\partial/\partial x' < \partial/\partial z'$ and $\partial/\partial x' < \partial/\partial y'$. The same conclusion applies to the distributions of w (data not shown). However, since the length scales used for estimating the gradients are significantly different, $\Delta y'/L \approx \Delta z/L \approx 0.0005$ and $\Delta x'/L \approx 0.036$, a ratio of 70:1, one must be cautious when applying this conclusion. The local gradients may be significantly higher. Before concluding, figure 21(*c*) shows the slope of the free surface in the x'-direction. The small angle supports our assumption that $u_{n'} = 0$.

4.2. *Vorticity production*

Longuet-Higgins (1992, 1994) and Duncan *et al*. (1994) demonstrated theoretically and experimentally the breaking process of a two-dimensional spilling breaking wave. They both show that as the wave becomes steeper, a bulge forms on its forward face and capillary waves form ahead of this bulge. According to Longuet-Higgins these capillary waves create a vortical region that causes local separation and eventually becomes turbulent. Duncan *et al*. however, observed that as the toe of the bulge moves down the forward face of the wave a train of large-amplitude, but short-wavelength, waves grow on the surface of this bulge. These waves grow rapidly and the flow becomes turbulent. These processes of spilling breaker formation have not been observed in the present study, although the existence of capillary waves near the wave crest has been evident in most of the present mild cases (see the samples in figures 2 and 3*b*, for example). The ship wave shown in these photographs is already 'broken', i.e. there is massive entrainment of vorticity generated at the free surface into the flow, especially near its toe, but as shown before, also along the crest. In some cases, such as the shoulder waves shown in figures 11 and 12, the wave slope is very mild, but vorticity entrainment at the toe is already significant. It is likely, however, as Lin & Rockwell (1995) observe, that the process described by Longuet-Higgins occurs during early stages of the ship motion, whereas the measurements are performed when the near-surface flow is already quite turbulent and 'steady' in the average sense. We would still like to relate the rate of vorticity entrainment to the main flow features.

A clue to the mechanism causing entrainment of free-surface vorticity is provided in recent papers by Rood (1994, 1995) and Dabiri & Gharib (1997). By manipulating the vorticity transport equation they bring it to a form that enables identification of specific flow phenomena that cause enhanced viscous diffusion of vorticity away from the free surface. Dabiri & Gharib use these expressions to measure the entrainment of vorticity in a two-dimensional spilling breaker. They show that viscous diffusion of the vorticity is associated with rapid acceleration and deceleration of the flow parallel to the free surface. In their case, most of this diffusion occurs just upstream of the toe of the spilling breaker and the amount of entrained vorticity matches well with the diffusion rate computed from their data. In order to explain the relationship between free-surface acceleration in vorticity entrainment, the momentum equation is written in the form (Panton 1984)

$$\frac{\partial u_i}{\partial t} + u_j \frac{\partial u_i}{\partial x_j} + \frac{1}{\rho}\frac{\partial p}{\partial x_i} - g_i = -\nu e_{ijk}\frac{\partial \omega_k}{\partial x_j}, \tag{7}$$

where u_i and ω_i are the velocity and vorticity, respectively. In the ship frame of reference, which will require us to subtract the ship speed from each velocity

component (see the sample in figure 17), the main features of the flow can be assumed to be steady and the unsteady term can be neglected. This assumption relies on the trends observed in the extended-exposure photographs and is less valid when the flow becomes turbulent downstream of the bow wave. Secondly, surface tension is neglected, namely the pressure is constant along the surface. Rewriting the surface-parallel component of equation (1), using curvilinear coordinates (s, n, x) (s and n are parallel and normal to the intersection of the laser sheet with the free surface, respectively, and x, is normal to the illuminated plane – see figure 1), leads to the following equation for the viscous vorticity flux near the free surface:

$$\left(u_i\frac{\partial v}{\partial x_i}\right)\cos\beta-\left(u_i\frac{\partial w}{\partial x_i}\right)\sin\beta-g\cos 38^\circ\sin\beta\approx-\nu\left(\frac{\partial\omega_x}{\partial n}-\frac{\partial\omega_n}{\partial x}\right), \tag{8}$$

where $\beta=-\tan^{-1}(\partial z/\partial y|_{surface})$. Unfortunately, PIV provides data only on the planar velocity distribution, i.e. u and $\partial/\partial x$ are unknown. To deal with this problem we have two options: the first is to examine the effect of the terms that we do know, and the second is to use the conclusions of the previous section in order to estimate the unknown terms. We opted to do both, i.e. look first at the distributions of known terms and then for one example add the effect of the estimated terms. As will be shown shortly, both are quite illuminating. The terms on the right-hand side represent viscous flux. The first is flux of ω_x across the boundary and the second is flux of ω_n normal to the laser sheet. However, since $\partial/\partial x'$ is typically small (see discussion in the previous section) then

$$\partial/\partial x\approx-\tan 38^\circ\,\partial/\partial z. \tag{9}$$

Since
$$\partial/\partial z=(\partial/\partial n)\cos\beta-(\partial/\partial s)\sin\beta, \tag{10}$$

and when multiplied by the viscosity it is unlikely that the tangential gradient, $\partial/\partial s$, is significant, then

$$\partial\omega_n/\partial x\approx-\tan 38^\circ\cos\beta\,\partial\omega_n/\partial n. \tag{11}$$

Thus, both terms on the right-hand side represent viscous flux of vorticity across the boundary. We can only measure the relationship between the acceleration and the distribution of ω_x. We opted to perform the analysis on the mild wave at $X/L=0.1$ (figure 9) and 0.14 (figure 10) that represent different levels of vorticity entrainment, and within the liquid sheet of the steep wave at $X/L=0.08$ (figure 14). The sum of the in-plane components of the acceleration in (8) is defined as a_s and the projection of the gravity is g_s, i.e.

$$a_s=\left(v\frac{\partial v}{\partial y}+w\frac{\partial v}{\partial z}\right)\cos\beta-\left(v\frac{\partial w}{\partial y}+w\frac{\partial w}{\partial z}\right)\sin\beta,\quad g_s=g\cos 38^\circ\sin\beta. \tag{12}$$

Detailed information on the distributions of all the terms in (9) for the first case ($X/L=0.1$, $Fr_L=0.279$), along with the measured free-surface contour and vorticity distribution are provided in figure 22(*a–c*). The results clearly show that a_s (figure 22*c*), is positive at $y/L>0.0418$, and that it peaks at the toe of the wave ($y/L=0.05$). Near the wave crest, a_s becomes negative for a short distance, and then changes again to positive with a second peak at $y/L=0.034$. Near the body a_s is positive, but small. When combined with gravity (figure 22*c*), the results suggest that there is negative vorticity flux at $y/L>0.0435$, with a peak still at the toe. There is weak positive flux all along the forward face of the wave and its crest, high negative flux on the back side

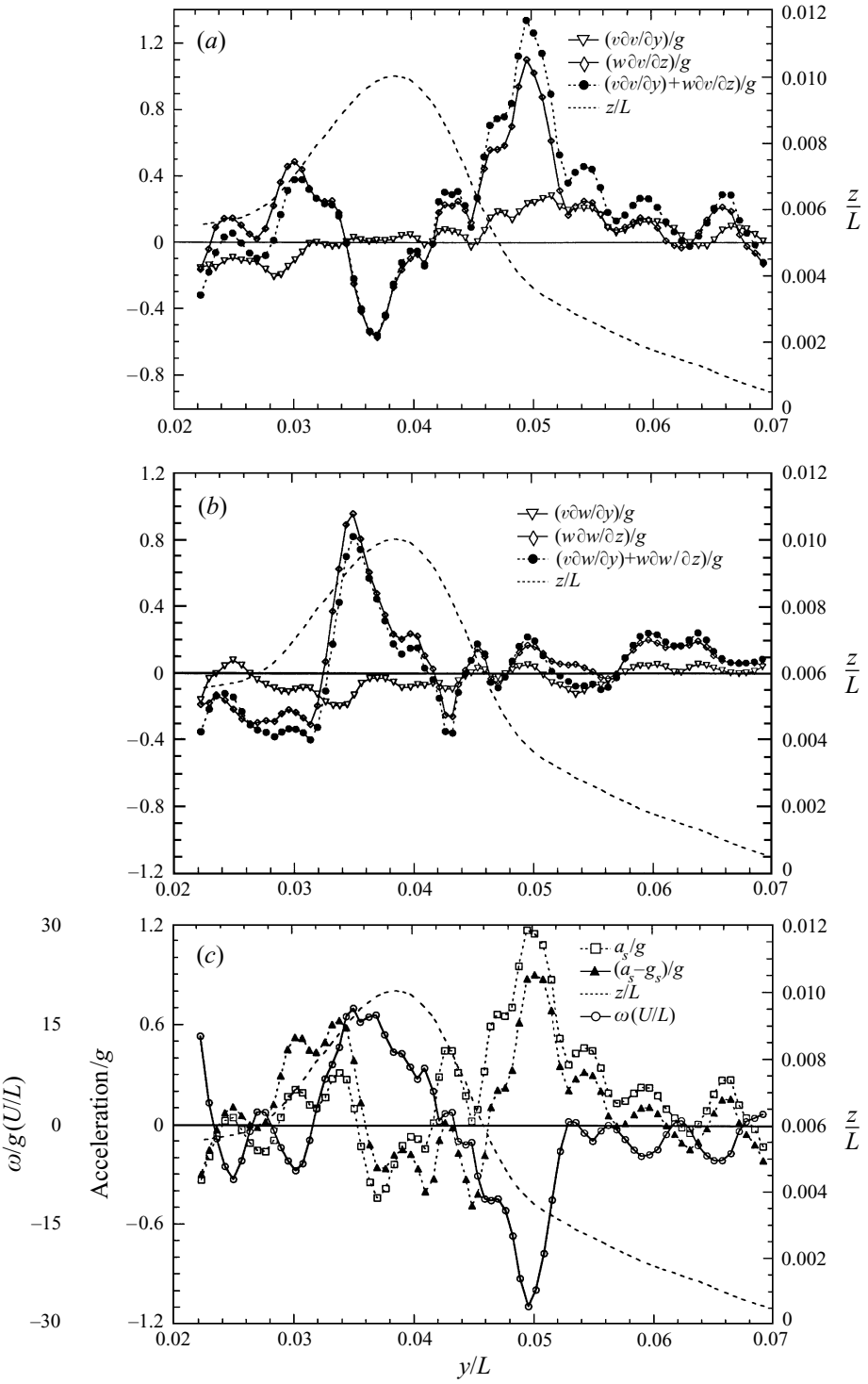

FIGURE 22. (*a*, *b*) Distribution of terms used for computing the near-surface acceleration at $X/L = 0.10$ and $Fr_L = 0.279$; (*c*) Distributions of a_s/g (the tangential acceleration components that can be computed using the velocity distribution within the laser sheet), $(a_s - g_s)/g$ and the vorticity distribution along the free surface.

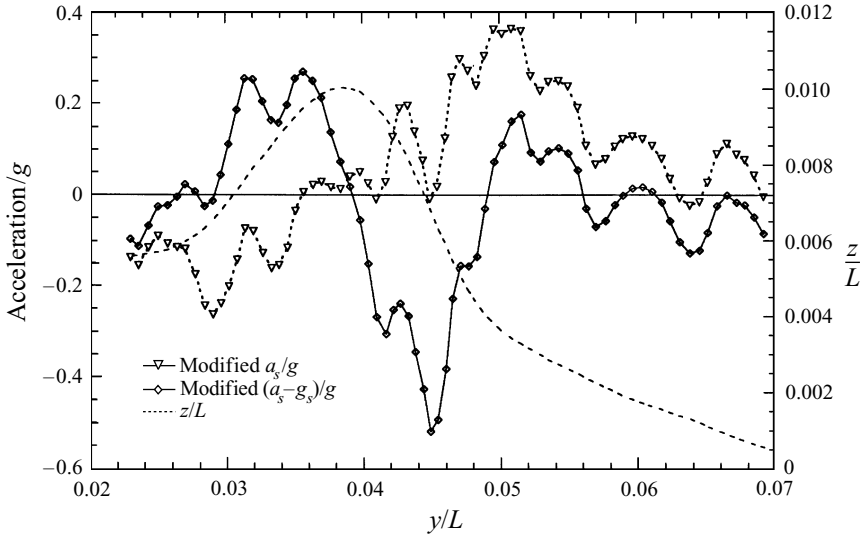

FIGURE 23. The distributions of the 'modified a_s/g' and 'modified $(a_s-g_s)/g$' (the tangential acceleration assuming that $\partial/\partial x'$ is small) at $X/L = 0.10$ and $Fr_L = 0.279$.

and positive flux very close to the model. The computed viscous vorticity flux is compared to the vorticity distribution along the surface in figure 22(*c*). It is evident that ω_x reaches a maximum negative value slightly to the left of the peak of negative flux. It then decreases in magnitude, consistent with the change in the sign of the flux and continues to increase until the computed surface flux becomes negative again. Then ω_x decreases again and fluctuates at a relatively low level until very close to the model, where it increases as the flux changes sign. Thus, there is an obvious agreement in trends between the distribution of the near-surface vorticity and the estimated viscous vorticity flux (based on in-plane components of the acceleration). These results suggest that viscous vorticity flux (near-surface acceleration) at and to the right of the toe is responsible for the entrained negative vorticity within the wave, and that flux of positive vorticity at the forward face and crest of the wave cause the formation of the positive peak at the wave crest. As (a_s-g_s) changes sign abruptly to the left of the crest, the positive vorticity near the wave crest disappears.

It should be noted here that since the flow is three-dimensional, and since the velocity component normal to the laser sheet is large and variable, the vorticity located at a certain plane away from the surface (figure 9) is a result of production at some location upstream of the laser sheet. Related formation of vortex filaments that extend from the wave crest has been demonstrated before. It is, however, reasonable to assume that the vorticity very close to the surface is produced very close to the laser sheet if not within it. Thus, one should expect a strong relationship between vorticity flux and its magnitude near the free surface. However, there is no clear correlation between the extent of viscous diffusion and the total amount of vorticity in the same plane. Such an agreement should be expected only in two-dimensional flows, as was demonstrated by Dabiri & Gharib (1997) for a hydraulic jump. In their case the viscous diffusion of vorticity occurred mostly in regions of abrupt decrease in the tangential velocity near the surface. In the present case the accelerations are considerably milder, and abrupt changes have only been observed in the steep bow wave case (similar to figure 15). Owing to these low acceleration levels, the effect of gravity on the present analysis is significant.

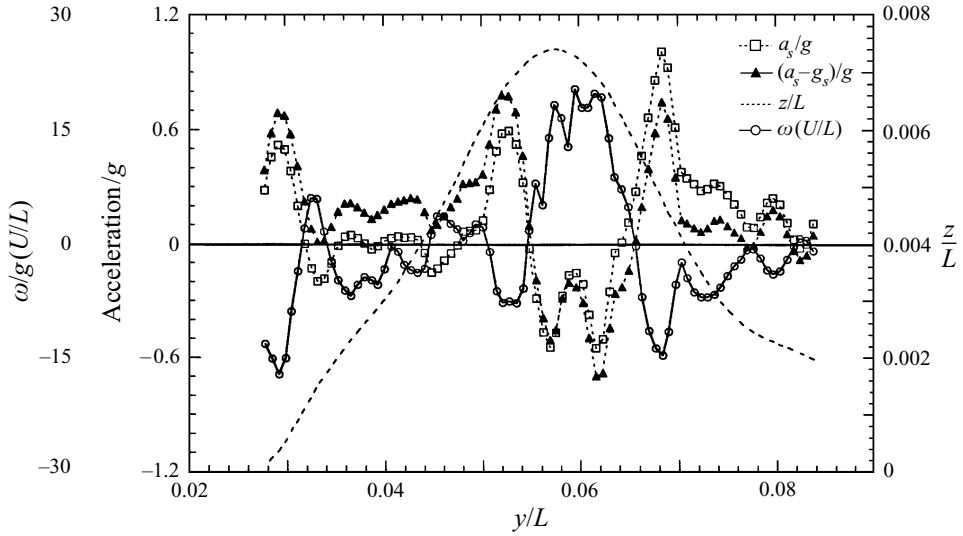

FIGURE 24. Distributions of a_s/g (the tangential acceleration components that can be computed using the velocity distribution within the laser sheet), $(a_s - g_s)/g$ and the vorticity distribution along the free surface at $X/L = 0.14$ and $Fr_L = 0.279$.

Next, using the conclusions of §4.2, namely that $\partial/\partial x' < \partial/\partial z'$, $\partial/\partial x' < \partial/\partial y'$ and $u^{n'} = 0$, then

$$\partial v/\partial x \approx -\tan 38^\circ \, \partial v/\partial z; \quad \partial w/\partial x \approx -\tan 38^\circ \, \partial w/\partial z \tag{13}$$

and using (1)–(4)

$$u \approx \frac{w}{\tan 38^\circ} + \frac{v \tan \beta'}{\sin 38^\circ}. \tag{14}$$

Thus, the missing terms on the left-hand side of (8), $u\,\partial v/\partial x$ and $u\,\partial w/\partial x$, can be estimated. The distribution of the complete tangential near-surface acceleration, identified as the 'modified a_s' is presented in figure 23. Here the positive peaks at the toe and behind the crest are considerably smaller, whereas the negative region in the forward face remains at the same level. Thus, in terms of trends, the conclusions based on a_s only or on the presumably more appropriate 'modified a_s' remain unchanged. However, the acceleration distribution in figure 23 suggests that there is more flux of positive vorticity at the upper, forward face of the wave than flux of negative vorticity at the toe. This trend may be the explanation for the vorticity distributions within the wave further away from the model, as shown in figure 10(*c*) in particular.

Trends in the in-plane components of the near-surface acceleration at $X/L = 0.14$ (figure 24) in the forward face and crest of the wave are similar to those at $X/L = 0.10$. There is still a smaller positive peak close to the toe, negative a_s at a higher magnitude to the right of and at the wave crest, and an abrupt change to a second positive peak to the left of the crest. These trends are consistent with the lower negative near-surface vorticity peak at the toe of the wave (figure 24*b*), higher positive vorticity near the wave crest and the reappearance of negative vorticity to the left of the crest. The vorticity away from the surface in this plane (figure 10) is considerably lower, suggesting that production upstream of, but close to, this plane is already considerably lower than the production upstream of $X/L = 0.1$. There is also a clear difference between these planes (figures 22*c* and 24) near the intersection of the model with the free surface. At $X/L = 0.1$ the acceleration becomes negative and the vorticity positive, whereas at

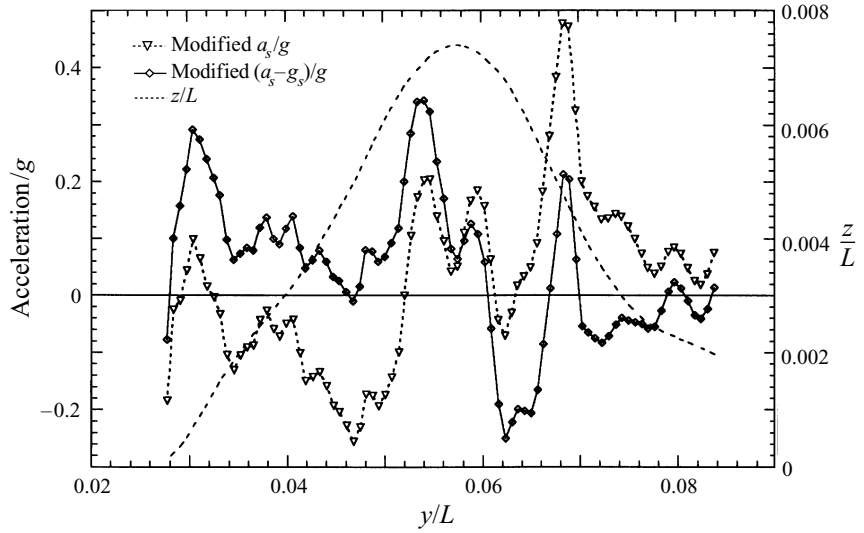

FIGURE 25. The distributions of the 'modified a_s/g' and 'modified $(a_s-g_s)/g$' (the tangential acceleration assuming that $\partial/\partial x'$ is small) at $X/L = 0.14$ and $Fr_L = 0.279$.

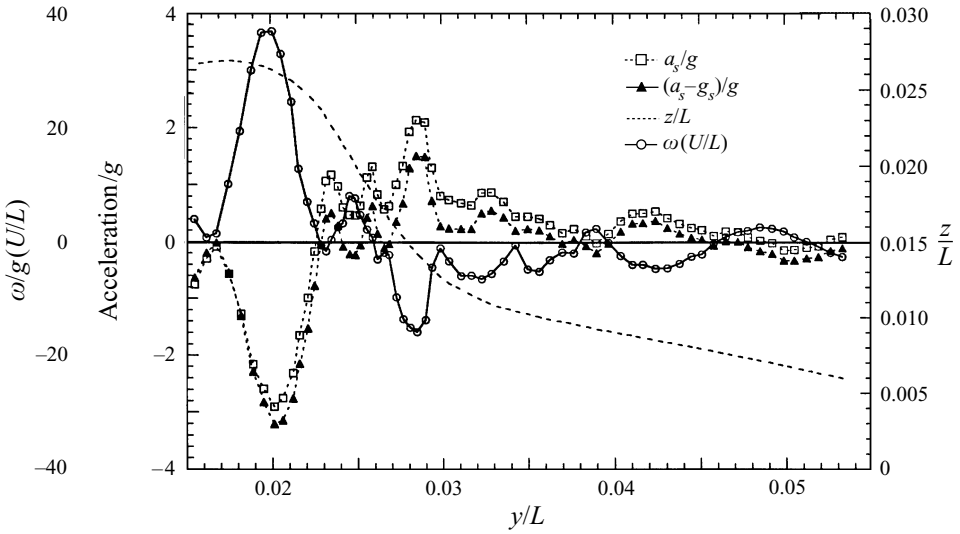

FIGURE 26. Distributions of a_s/g (the tangential acceleration components that can be computed using the velocity distribution within the laser sheet), $(a_s-g_s)/g$ and the vorticity distribution along the free surface at $X/L = 0.08$ and $Fr_L = 0.446$.

$X/L = 0.14$ there are clear additional positive acceleration and negative vorticity peaks. As noted before, by examining the top-view photograph (figure 4*b*) it becomes evident that the $X/L = 0.14$ sheet intersects with the ship model at the origin of the shoulder wave. Thus, the peaks in a_s and vorticity occur at the toe of the shoulder wave whose formation involves considerable negative vorticity production (figures 10–12). When a_s is modified to account for $u\partial v/\partial x$ and $u\partial w/\partial x$ (figure 25) the conclusions remain unchanged, but the magnitude of the estimated vorticity diffusion are reduced.

The acceleration, effect of gravity and comparisons to the distribution of near-surface vorticity for the flow within the sheet of the steep wave, at $X/L = 0.08$, are presented in figures 26(*a*) and 26(*b*), respectively. There is a relatively small positive

acceleration peak at the toe of the sheet (which is still larger than the mild wave data – note the difference in scales) and a giant negative peak, with magnitude exceeding 3 g slightly to the right of the tip of the sheet. Trends in the distribution of near-surface vorticity are completely consistent with the estimated viscous diffusion. There is a weaker negative vorticity peak near the toe and a large positive peak at the crest of the sheet. In this particular case, the dominant term that affects both the vorticity and near-surface acceleration is $\partial v/\partial z$, although $v\,\partial v/\partial y$ is also significant in the acceleration term. As shown before (figure 14*b*), the flow near the outer face of the tip of the sheet contains a considerable amount of positive vorticity. The analysis shows that production of this vorticity is associated with rapid deceleration of the flow near the free surface. Unlike the mild wave, we made no attempt to estimate the effects of $u\,\partial v/\partial x$ and $u\,\partial w/\partial x$ within the sheet, mostly since they do not alter the conclusions and it is not clear that the underlying assumptions are valid in this case.

5. Summary and conclusions

PIV measurements and free-surface visualizations around a ship model focused on the flow within the liquid sheet forming around the bow, the origin of the bow wave, variation in the structure of this wave at different distances from the model and the flow near the body downstream of the wave. The measurements were performed at Reynolds numbers ranging from 2.8×10^6 to 7.4×10^6 and Froude numbers, based on ship length, from 0.17 to 0.45. Representative data at $Fr_L = 0.28$ demonstrated the characteristic structure of a mild wave, and a second set, at $Fr_L = 0.45$, showed the structure of a steep wave, whose forward face was vertical shortly before plunging and entraining bubbles. In spite of the different Froude numbers and wave shapes, these flows had several common characteristics that became more pronounced and easier to identify with increasing Froude number.

Photographs of the wave structure demonstrated the formation of a thin liquid sheet on the body upstream of the point at which the bow wave separated from the model. Very close to the bow the sheet was very thin – not more than 2 mm wide – and was quite unsteady, fluctuating in elevation and thickness. The thickness of the sheet increased with increasing distance from the nose and its formation involved considerable vorticity production. In the mild case the dominant source of this vorticity was located at the free surface. In the steep wave case, boundary layer separation occurred on the surface of the model, which also transported vorticity into the sheet. Negative vorticity was entrained into the flow close to the toe of the liquid sheet. A submerged shear layer that started at the toe extended into the flow, along what appeared to be the interface between the liquid sheet and forward face of the bow wave. By calculating the acceleration component tangent to the free surface it was shown that the peaks in the near-surface vorticity, particularly at the toe and the tip of the sheet, appeared in regions with high viscous flux of vorticity from the surface. At the tip of the sheet the deceleration exceeded -3 g, whereas at the toe, the acceleration was larger than 2 g.

The results also demonstrated that vorticity produced within the liquid sheet remained near the surface of the model downstream of the bow wave. In the steep case this vorticity produced secondary flows with high lateral velocities (up to 20 % of the ship speed), whose impact could be easily sensed at $X/L = 0.24$.

In both the mild and steep cases, the formation of a bow wave involved considerable production of vorticity. Similar to the structure of two-dimensional spilling breakers (Banner & Peregrine 1993; Lin & Rockwell 1994, 1995; Dabiri & Gharib 1997) the

primary origin of this vorticity was at the toe of the breaker. However, unlike the two-dimensional waves, most of the vorticity remained close to the forward face of the wave and only a small portion extended into the liquid to form a submerged shear layer. Furthermore, the ship wave had a powerful counter-rotating vortical structure that was concentrated near the wave crest. The existence of vorticity with opposite sign has already been observed in two-dimensional waves, but not at the present strength and area. The vorticity generated at a wave crest was fed into the flow behind in a series of distinct filaments, that created a series of elongated 'bumps' on the free surface. A sample cross-section of the flow within a 'bump' showed that it consisted of a pair of counter-rotating vortices. However, some bumps contained a single vortex. Breaking became weaker, i.e. there was much less vorticity diffusion at the toe, with increasing distance from the model. However, some negative vorticity entrainment occurred even at the 'tail' of the bow wave. The positive vorticity diffusion close to the wave crest persisted throughout the entire wave at a similar level. The shoulder wave that followed showed similar trends, i.e. entrainment of negative vorticity even when the wave slope was very mild. In the steep case, the bow wave plunged and created a bubbly wake. The present study focuses on the flow prior to plunging, but future studies will focus on this phenomenon.

The acceleration component tangent to the free surface, computed from the measured velocity distributions, showed clear consistency between the computed distributions of viscous vorticity flux from the free surface and the distributions of high near-surface vorticity. Entrainment of positive vorticity occurred in regions with negative acceleration (relatively to the ship), such as the wave crest, whereas negative vorticity was entrained at the toe, where the acceleration relatively to the ship was positive. In the present cases the effect of gravity was significant.

By assuming that the velocity component normal to the water surface was zero (steady flow) and using the fact that the present light sheets were inclined, it was possible to estimate all three components of the velocity and energy losses along the surface. Trends agreed for the most part with Miyata & Inui's (1984) data. The results showed that considerable energy loss ($\sim 30\%$ of the total head) occurred in the forward face of the wave, especially near the toe. This conclusion was consistent with the occurrence of flow separation and vorticity entrainment at the same location. They also demonstrated the abrupt change in flow direction away from the ship in the forward face of the wave (maximum change was at the crest), and turning back of the flow towards the model behind the wave. This flow towards the body causes the formation of the shoulder wave.

This work is supported by the Office of Naval Research under grant number N00014-93-1-0204. The program manager is Dr Edwin Rood. Thanks are also due to E. Pogozelski for his help in setting the experiments, and to T. Fu and H. Liu for helping us to find the model.

REFERENCES

Adrian, R. J. 1991 Particle-imaging techniques for experimental fluid mechanics. *Ann. Rev. Fluid Mech.* **23**, 261–304.

Banner, M. L. & Peregrine, D. H. 1993 Wave breaking in deep water. *Ann. Rev. Fluid Mech.* **25**, 373–397.

Cointe, R. & Tulin, M. P. 1994 A theory of spilling breakers. *J. Fluid Mech.* **276**, 1–20.

Dabiri, D. & Gharib, M. 1997 Experimental investigation of the vorticity generation within a spilling water wave. *J. Fluid Mech.* **330**, 113–139.

Dommermuth, D. G. 1993 The laminar interaction of a pair of vortex tubes with a free surface. *J. Fluid Mech.* **246**, 91–115.

Dommermuth, D. G. & Mui, R. 1994 The vortical structure of a wave breaking gravity-capillary wave. *12th Symp. on Naval Hydrodynamics*, *Santa Barbara*, *CA*.

Dommermuth, D. G., Yue, K. P., Lin, W. M., Rapp, W. M., Chan, E. S. & Melville, W. K. 1988 Deep water plunging breakers: a comparison between potential theory and experiments. *J. Fluid Mech.* **189**, 423–442.

Dong, R., Chu, S. & Katz, J. 1992 Quantitative visualization of the flow structure within the volute of a centrifugal pump, Part A: Technique. *Trans. ASME: J. Fluids Engng* **114**, 390–395.

Duncan, J. H., Philomin, V., Behres, M. & Kimmel, J. 1994 The formation of spilling breaking water waves. *Phys. Fluids* **6**, 2558–2560.

Fry, D. J. & Kim, Y. H. 1984 Bow flow of surface ships. *Proc. 15th Symp. on Naval Hydrodynamics, Hamburg Germany*, pp. 319–346.

Fu, T., Shekarriz, R., Katz, J. & Huang, T. T. 1994 The flow structure in the lee of an inclined 6:1 prolate spheroid. *J. Fluid Mech.* **269**, 79–106.

Hoyt, J. W. & Sellin, R. H. T. 1989 The hydraulic jump as a mixing layer. *J. Hydraul. Div. ASCE* **115**, 1607–1614.

Lin, J. C. & Rockwell, D. 1994 Instantaneous structure of a breaking wave. *Phys. Fluids* **6**, 2877–2879.

Lin, J. C. & Rockwell, D. 1995 Evolution of a quasi-steady breaking wave. *J. Fluid Mech.* **302**, 29–44.

Longuet-Higgins, M. S. 1992 Capillary rollers and bores. *J. Fluid Mech.* **240**, 659–679.

Longuet-Higgins, M. S. 1994 The initiation of spilling breakers. *Intl Symp: Waves – Physical and Numerical Modeling*, *University of British Columbia*, *Vancouver*, *Canada*, *August 21–24*, pp. 24–48.

Lugt, H. 1987 Local flow properties at a viscous free surface. *Phys. Fluids* **30**, 3647–3652.

Melville, W. K. & Rapp, W. M. 1988 The surface velocity field in steep and breaking waves. *J. Fluid Mech.* **189**, 1–22.

Miyata, H. & Inui, T. 1984 Nonlinear ship waves. *Adv. Appl. Mech.* **24**, 215–288.

Panton, R. L. 1984 *Incompressible Flow*. J. Wiley & Sons.

Peregrine, D. H. & Svendsen, I. A. 1978 Spilling breakers, bores, and hydraulic jumps. *Proc. 16th Coastal Engng Conf. ASCE*, *Hamburg*, Vol. 1, pp. 540–550.

Pogozelski, E. M., Katz, J. & Huang, T. 1996 The flow structure around a surface piercing strut. *Phys. Fluids.* **9**, 1387–1399.

Rood, E. P. 1994 Interpreting vortex interactions with a free surface. *Trans. ASME: J. Fluids Engng* **116**, 91–94.

Rood, E. P. 1995 Sources of vorticity on the shear free-surface boundary of viscous, irrotational flows. *ASME Symp. on The Interaction of Surface Waves*, *Currents*, *Bodies*, *and Wakes at or Near a Free Surface*, *San Francisco*, *CA*.

Roth, G., Hart, D. & Katz, J. 1995 Feasibility of using the L64720 video motion estimation processor (MEP) to increase efficiency of velocity map generation for PIV. *ASME/EALA Sixth International Symposium on Laser Anemometry*, *Hilton Head SC*, *August*, 13–18, pp. 387–393.

Sarpkaya, T. 1996 Vorticity, free surface and surfactants. *Ann. Rev. Fluid Mech.* **28**, 83–128.

Sarpkaya, T. & Sutton, P. B. R. 1991 Interaction of a vortex couple with a free surface. *Exps. Fluids* **11**, 205–217.

Tryggvason, G. 1988 Deformation of a free surface as a result of vortical flows. *Phys. Fluids* **31**, 955–957.

Yu, D. & Tryggvason, G. 1990 The free surface signature of unsteady, two-dimensional vortex flows. *J. Fluid Mech.* **218**, 547–572.